APRIL 1992

ORNL/Sub/84-89628/04

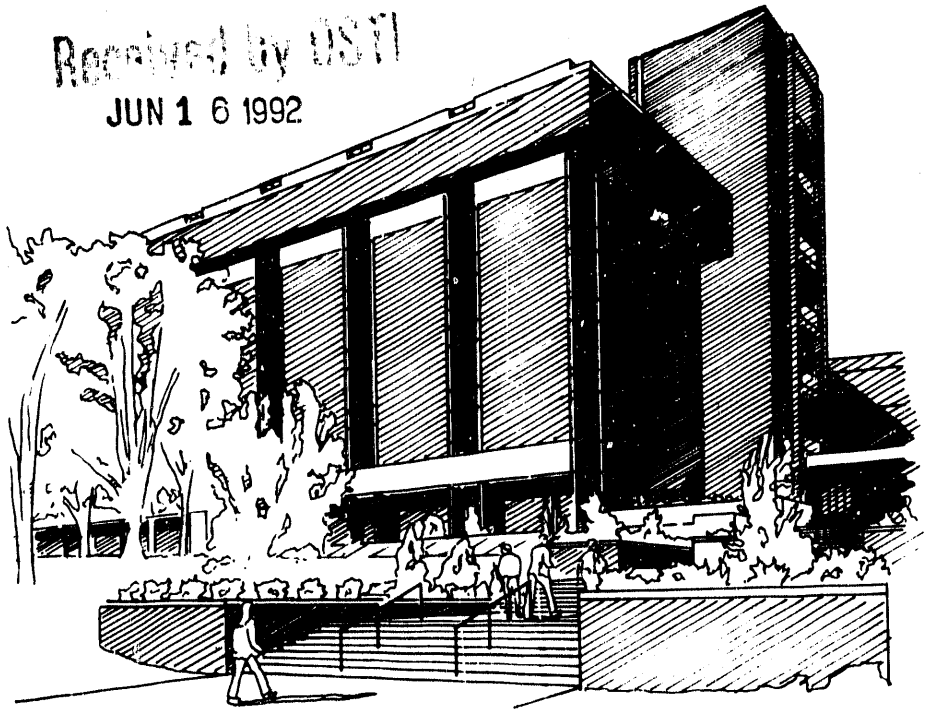

UNIVERSITY OF CINCINNATI
COLLEGE OF ENGINEERING

Department of Aerospace Engineering and Engineering Mechanics
Cincinnati, Ohio 45221

STUDY OF PARTICLE REBOUND CHARACTERISTICS AND MATERIAL EROSION AT HIGH TEMPERATURE

Report Prepared by

W. Tabakoff, A. Hamed, A. Metwally, J. Yeuan

Under
Subcontract No. 19X-89628C
B&R Code AA 15 10 10 0

for
OAK RIDGE NATIONAL LABORATORY
Oak Ridge, Tennessee 37831
managed by
MARTIN MARIETTA ENERGY SYSTEMS, INC.
for the
U. S. DEPARTMENT OF ENERGY
under Contract No. DE-AC05-84OR21400

STUDY OF PARTICLE REBOUND CHARACTERISTICS AND MATERIAL EROSION AT HIGH TEMPERATURE

ORNL/Sub--84-89628/04

DE92 015544

April 1992

Research sponsored by the U.S. Department of Energy,
Fossil Energy
Advanced Research and Technology Development Materials Program

Report Prepared by

W. Tabakoff, A. Hamed, A. Metwally, J. Yeuan

University of Cincinnati
Department of Aerospace Engineering and Engineering Mechanics
Cincinnati, Ohio 45221

Under
Subcontract No. 19X-89628C

B&R Code AA 15 10 10 0

for

OAK RIDGE NATIONAL LABORATORY
Oak Ridge, Tennessee 37831
managed by
MARTIN MARIETTA ENERGY SYSTEMS, INC.
for the
U. S. DEPARTMENT OF ENERGY
under Contract No. DE-AC05-84OR21400

TABLE OF CONTENTS

	Page
LIST OF TABLES	ii
LIST OF FIGURES	iii
NOMENCLATURE	vi
ABSTRACT	1
INTRODUCTION	2
EXPERIMENTAL SET-UP	4
Erosion Wind Tunnel	4
Solid Particles Rebound Facility	5
TEST CONDITIONS AND TEST MATERIALS	7
RESTITUTION TEST RESULTS	7
THEORETICAL MODEL OF SOLID PARTICLE IMPACT ON A TARGET OF DUCTILE MATERIAL	13
Introduction	13
Theoretical Formulation	13
Results and Discussion	17
EROSION TEST RESULTS	18
Impingement Angle Effect on the Erosion Rate	18
Comparison Between 410 Stainless Steel and Coatings Erosion Rates	20
Velocity Effect on Erosion Rates	21
Temperature Effect on the Erosion Rate	21
DUCTILE EROSION RATE MODEL	22
Erosion Model at Low Impingement Angle	22
Erosion Model at Normal Impact	25
Prediction of the Superalloy and Coating Erosion Rates	26
PARTICLE TRAJECTORIES AND BLADE EROSION IN A TWO-STAGE TURBINE BASED ON REBOUND AND EROSION MODELS	29
Particle Trajectories	29
Blade Surface Erosion	30
REFERENCES	32
TABLES	34
FIGURES	38
DISTRIBUTION	75

LIST OF TABLES

Table	Title	Page
1	LDV Characteristics	34
2	Tested Superalloys	34
3	The Tested Coatings	35
4	Chemical Analysis of Fly Ash	35
5	Typical Chromite Powder Analysis	36
6	Material Coefficients of Erosion Models	37

LIST OF FIGURES

Figure		Page
1	Schematic of Erosion Test Facility	38
2	Schematic of Rebound Test Facility	39
3	Schematic of LDV Experimental Set-Up	40
4	Rebound Velocity and Angle Notation	41
5	Fly Ash Particle Size Distribution	41
6	Normal Velocity Restitution Ratio Distribution	42
7	Tangential Velocity Restitution Ratio Distribution	42
8	Directional Restitution Ratio Distribution	43
9	Total Velocity Restitution Ratio Distribution	43
10	Tangential Velocity Restitution Ratio of M246 Alloy and N, RT22 and RT22B Coatings: V_1 = 320 fps, Fly Ash Particles	44
11	Normal Velocity Restitution Ratio of M246 Alloy and N, RT22 and RT22B Coatings: V_1 = 320 fps, Fly Ash Particles	44
12	Total Velocity Restitution Ratio of M246 Alloy and N, RT22 and RT22B Coatings: V_1 = 320 fps, Fly Ash Particles	45
13	Directional Restitution Ratio of M246 Alloy and N, RT22 and RT22B Coatings: V_1 = 320 fps, Fly Ash Particles	45
14	Tangential Velocity Restitution Ratio of X40 Alloy and C, RT44 and RT44B Coatings: V_1 = 320 fps, Fly Ash Particles	46
15	Normal Velocity Restitution Ratio of X40 Alloy and C, RT44 and RT44B Coatings: V_1 = 320 fps, Fly Ash Particles	46
16	Total Velocity Restitution Ratio of X40 Alloy and C, RT44 and RT44B Coatings: V_1 = 320 fps, Fly Ash Particles	47
17	Directional Restitution Ratio of X40 Alloy and C, RT44 and RT44B Coatings: V_1 = 320 fps, Fly Ash Particles	47
18	Particle Rebound Velocity Variation with Impact Velocity for Different Impact Angles	48
19	Particle Rebound Angle Variation with Impact Velocity for Different Impact Angles	48
20	Particle Kinetic Energy Loss Variation with Impact Velocity for Different Impact Angles	49

21	Chromite Particle Size Distribution	50
22	410 Stainless Steel Erosion Rate Variation with Impingement Angle: T=1022 F, Chromite Particles	50
23	LC-1B Coating Erosion Rate Variation with Impingement Angle: T = 1022 F, Chromite Particles	51
24	LC1-1H Coating Erosion Rate Variation with Impingement Angle: T=1022 F, Chromite Particles	51
25	Plasma Spray Coating Erosion Rate Variation with Impingement Angle: T = 1022 F, Chromite Particles	52
26	SDG-2207 Coating Erosion Rate Variation with Impingement Angle: T=1022 F, Chromite Particles	52
27	Comparison of Erosion Rates of Coatings and 410 Stainless Steel Alloy: β_1=30°, Chromite Particles	53
28	Comparison of Erosion Rates of Coatings and 410 Stainless Steel Alloy: β_1=90°, Chromite Particles	53
29	Velocity Effect on 410 Stainless Steel Erosion Rate at Different Angles: T=1022 F, Chromite Particles	54
30	Velocity Effect on LC-1B Coating Erosion Rate at Different Angles: T = 1022 F, Chromite Particles	55
31	Velocity Effect on LC-1H Coating Erosion Rate at Different Angles: T = 1022 F, Chromite Particles	56
32	Velocity Effect on Plasme Spray Coating Erosion Rate at Different Angles: T = 1022 F, Chromite Particles	57
33	Velocity Effect on SDG-2207 Coating Erosion Rate at Different Angles: T = 1022 F, Chromite Particles	58
34	Variation of Erosion Rate with Temperature for LC-1B, LC-1H, SDG-2207 and Plasma Spray Coatings and 410 Stainless Steel: V_1=750 fps, Chromite Particles	59
35	Schematic of Theoretical and Actual Erosion Process	60
36	Comparison Between Measured and Predicted Erosion Rates for FSX-414 Alloy	61
37	Comparison Between Measured and Predicted Erosion Rates for IN-738 Alloy	61
38	Comparison Between Measured and Predicted Erosion Rates for M246 Alloy	62

39	Comparison Between Measured and Predicted Erosion Rates for X40 Alloy	62
40	Variation of Superalloy Temperature Parameters with Temperature	63
41	Comparison Between Measured and Predicted Erosion Rates for N Coating	63
42	Comparison Between Measured and Predicted Erosion Rates for RT22 Coating	64
43	Comparison Between Measured and Predicted Erosion Rates for RT22B Coating	64
44	Projection of Particle Trajectories in θ-z Plane	65
45	Projection of Particle Trajectories in r-z Plane	67
46	Impact Location for the Uniform Particles	69
47	Impact Locations for the Individual Particle Sets First Rotor	70
48	1st Stator Pressure Surface Erosion Rate $x10^5$ (mgm/gm/cm^2)	71
49	1st Rotor Pressure Surface Erosion Rate $x10^5$ (mgm/gm/cm^2)	72
50	2nd Stator Pressure Surface Erosion Rate $x10^5$ (mgm/gm/cm^2)	73
51	2nd Rotor Pressure Surface Erosion Rate $x10^5$ (mgm/gm/cm^2)	74

NOMENCLATURE

A	Elemental area
a, c	Constant
C_{11}, C_{22}, C_0	Empirical constant
D_T	Particle tangential displacement
e_N	Normal restitution ratio
e_T	Tangential restitution ratio
e_V	Total velocity restitution ratio
e_β	Directional restitution ratio
h	Crater depth
M_p	Mass of a particle
P	Hydrostatic pressure
q	Artificial viscosity
S	Deviatoric stress
t	Time
V, v	Particle velocity
V_N	Normal velocity component
V_T	Tangential velocity component
Vol	Crater volume
V	Volume
x, y	Cartesian coordinates
Y_0	Yield strength
Y_{RT}	Yield strength at room temperature
β	Angle
δ	Rotation correction factor
Σ	Total stress
ϵ	Strain or erosion rate
μ, λ	Lame constant
ρ	Density
τ	Shear stress

Subscript	
T	Tangential
N	Normal
1	Impact
2	Rebound
t	Target
0	Static condition
xx,yy	x and y direction
Superscript	
•	Time derivative

RESEARCH SPONSORED BY U.S. DEPARTMENT OF ENERGY
FOSSIL ENERGY AR&TD MATERIALS PROGRAM
DOE/FE AA 15 10 10 0
WORK BREAKDOWN STRUCTURE ELEMENT UCIN-3

ABSTRACT

In this research an investigation was conducted to study the ash particle rebound characteristics and the associated erosion behavior of alloys and coatings which are widely used in gas and steam turbines. A three-component LDV system was used to measure the restitution parameters of 15 micron mean diameter coal ash particles impacting superalloys and coatings at different angles. The presented results show the variation of the particle restitution ratios with the impingement angle for the coated and uncoated surfaces. The experimental results were used to develop correlations for the restitution parameters for coated and uncoated superalloys. In addition, a theoretical model based on elastic-plastic theory has been developed to simulate single solid particle impacts on solid targets. The theoretical results are presented for a hard tool steel particle impacting a mild steel target. The results show the variation of rebound velocity, rebound angle and particle kinetic energy loss with impact velocity for oblique and normal impacts. The erosion behaviors of many alloys and protective coatings have also been investigated experimentally at high temperatures using a specially designed erosion tunnel. The erosion results show the effect of velocity, temperature and the impact angle on the erosion rate (weight loss per unit weight of particles). Erosion models were developed for these materials based on the experimental erosion data and correlations of the restitution parameters. The developed rebound and erosion models have been used to predict particle trajectories and blade erosion in a two stage turbine operating in particulated environments. The predicted results show the three dimensional particle trajectories through the turbine blade passages and the spacial distributions of the blade erosion over the pressure surfaces of the turbine blades.

INTRODUCTION

Gas and steam turbines operate in environments where the ingestion of solid particles is inevitable. In industrial applications and power generation, such as coal-burning boilers, fluidized beds and gas turbines, solid particles are produced during the combustion process of heavy oils, synthetic fuels and pulverized coal. In commercial and military aircrafts and naval installations, some of the mechanisms that cause solid particle ingestion are vortex generated during landing and takeoff, sand storms, volcanic ashes and thrust reverser efflux at low speed blows sand, ice and dust into the engines. In steam turbines, the solid particles are principally boiler scales, mainly iron oxide, that breaks off and becomes entrained in the steam. Filters and separators can remove a large percentage of the solid particles, but significant amounts of small particles still pass through and enter the engines.

Due to their higher inertia, the solid particles deviate from the flow streamlines, impact the blade surfaces and cause severe erosion damage. This damage is manifested by pitting and cutting of the blade leading and trailing edges and an increase in the blade surface roughness. The overall effects of the above phenomena are increase of pressure loss and change of the blade geometry. Continued operation under particulate flow conditions adversely affects the performance of the engines, as well as, their lives and can be detrimental to their reliability.

Gas turbine materials have developed rapidly beyond the conventional ferrous alloys consisting of steels and stainless steels of various compositions, physical, thermal and mechanical history and microstructure. Several nickel and cobalt base alloys were developed and have been used widely in the hot section of gas turbines in order to meet complex high temperature corrosion phenomena. Chromium additions have been used and contribute to an improvement in high temperature strength and oxidation resistance. Protective coatings have been used to enhance superalloy resistance to hot erosion-corrosion. Some of the mose widely used coatings are diffusion coatings, overlay coatings, plasma sprayed coatings and ion implantation coatings. Chromium, platinum, radium and silicon additions have been used in order to improve erosion-corrosion resistance of the coatings.

Although physical, chemical and mechanical properties of turbine alloys and coatings are documented satisfactorily, there is not enough data about their rebound and erosion behavior, especially at high temperature. Therefore, an experimental investigation has been conducted to study coal ash particle rebound characteristics and associated erosion behavior of many alloys and coatings subjected to particulate flows at high temperature. A 3-D LDV system was used to measure the restitution parameters of coal ash particles impacting alloys and coating at different angles. The experimental results were used to develop correlations for the restitution parameters for coated and uncoated alloy surfaces. These corelations can be used to model particle-surface interaction in theoretical studies. A theoretical model of single solid particle impact on a target of ductile material has been developed. The model is based on the elastic-plastic theory and Rankine-Hugonior relation. The predicted results are presented for 9.5 mm diameter hard steel particle impacting a target of mild steel at different impact angles. The erosion behaviors of alloys and protective coatings have been investigated experimentally at high temperature using a specially designed erosion tunnel. The erosion results show the effect of the main erosion parameter, namely, velocity, temperature and impact angle, on the erosion rates. Erosion models have been developed for the tested materials based on the experimental erosion data and restitution parameters. The developed rebound and erosion models have been used to predict particle trajectories and blade erosion in a two stage gas turbine for 15 micron weight average coal ash particles.

EXPERIMENTAL SET-UP

The experimental set-up consists of the following: a) the erosion wind tunnel, and b) solid particles rebound facility.

Erosion Wind Tunnel

The high temperature erosion test facility was designed to provide erosion and rebound data in the range of operating temperatures experienced in compressors and turbines. In addition to the high temperatures, the facility properly simulates the erosion parameters which were determined to be important from aerodynamic's point of view. These parameters include particle velocity, angle of impact, particle size, particle concentration, and sample size. Close attention was given to the aerodynamic effects to insure that important parameters, such as the angle of impact, are not masked or altered.

A schematic of the erosion test facility is shown in Fig. 1. It consists of the following components: particle feeder (A), main air supply pipe (B), combustor (C), particle preheater (D), particle injector (E), acceleration tunnel (F), test section (G), and exhaust tank (H).

The equipment functions as follows. A measured amount of abrasive grit of a given mixture of constituents is placed into the particle feeder (A). The particles are fed into a secondary air source and blown up to the particle preheater (D), and then to the injector (E), where they mix with the main air supply (B), which is heated by the combustor (C). The particles are then accelerated by the high-velocity air in a constant-area steam-cooled duct (F) and impact the specimen in the test section (G). The particulate flow is then mixed with the coolant and dumped in the exhaust tank. Figure 1 shows that the tunnel geometry is uninterrupted from the acceleration tunnel into the test section. In this manner the particle laden flow is channeled over the specimen and the aerodynamics of the fluid passing over the sample are preserved.

A detailed description of the wind tunnel and the particle feeder is given in Ref. [1].

Solid Particles Rebound Facility

The rebound facility consists of three main components: (i) rebound wind tunnel, (ii) Laser Doppler Velocimeter (LDV) system and (iii) data acquisition system.

Rebound Wind Tunnel:

The rebound wind tunnel is schematically shown in Fig. 2. The tunnel's main components are: particle feeder (A), main air supply (B), particle injector (C), acceleration tunnel (D), test section (D), exhaust filter (F), and cyclone (G). Tunnel aerodynamic design and functioning are similar to those of the erosion wind tunnel. This facility is capable to provide rebound data in the range of operating velocities experienced in gas turbines at room temperature. The test section has a transparent window through which the LDV measurements have been taken.

LDV System:

The LDV system used in the measurements of the particle restitution characteristics is shown schematically in Fig. 3 and described in detail in references [2] and [3]. It consists of a laser tube, optics, frequency shifters and the photo-multipliers. The light source is a five Watt argon-ion Spectra Physics, model 164-09 laser tube. The laser beam leaving the tube is separated in the dispersion prism into components with different wavelengths. Three beams with the highest intensities are used to measure the three velocity components. The two beams with green (0.5145 μm) and blue (0.488 μm) colors are sent through an optical train in the axial direction. The third beam with purple color (0.4765 μm) passes through a second optical train whose transmitting optics are inclined at 30 degrees from the axial direction. Each beam is polarized through a polarization rotator and split into two equal intensity components in the beam splitter. After passing through the focusing lenses, the two beams of each color cross and produce a set of fringes. Six beams cross at one common measuring volume producing three sets of fringes, one for each color. TSI model 9189 beam expanders were used to increase the spatial resolution, improve the single-to-noise ratio, and reduce the measurement volume diameter 3.75 times. Two separate beam collimaters, one on the blue-green optical train

and the other on the purple optical train, were installed before the beam splitters for precise control of the probe volume characteristics. In particular, it was possible to ensure that the focused beams intersected at their beam waists to avoid frequency broadening effects and maximize signal quality. The scattered light from the particles in the measuring volume is collected in the off-axis backward scatter mode. Frequency shifters were used on all the three beams to sense the flow direction and reduce fringe bias errors. The analog data from the photomultipliers in the receiving optics mixed with the signals from frequency shifters are transferred to three separate signal processors. The characteristics of the LDV system used are compiled in Table 1.

Data Acquisition System:

The data acquisition system consists of three signal processors, an external circuit and a personal computer with the associated hardware and software. While the data acquisition is software driven, the data timing is controlled by an external circuit. The LDV signals coming from the photomultipliers are processed in the three TSI 1990 counter type signal processors. The processed data are collected by an IBM PC/AT compatible computer for further calculations and data storage. The control of the data transfer and the synchronization of data coming from the three different channels are performed by the external circuit.

The logic for the data acquisition system is as follows: The frequency of the internal oscillator clock in the CTM-05 counter-timer is specified initially through the interactive software. This clock generates a square wave at the selected frequency and the period of the wave determines the coincidence window for the data coming from the processors connected to the three LDV channels. During the data collection, the external circuit is activated in order to detect the arrival of data ready signals. Whenever the external circuit receives a data ready pulse, it sends a data inhibit signal to the associated processor, preventing it from acquiring new data. When all the three data ready signals arrive within the specified coincidence limit, the circuit holds the data at the output buffers of the processors, and instructs the computer to transfer them into a file through the digital input port. The external circuit is then reset through the

digital output port of CTM-05, the processors are reactivated and the procedure is repeated until a specified number of samples is collected.

TEST CONDITIONS AND TESTED MATERIALS

It is well known that particle velocity, particle impingement angle, particle characteristics and material sample temperature strongly influence the erosion rate. These parameters were varied in the present test program for the different tested materials listed in Tables 2 and 3. The properties of the superalloys can be found in Refs. [4] and [5]. The particle velocity was controlled by varying the tunnel air flow. The particle impingement angle was set by rotating the sample relative to the flow stream direction. The sample temperature was varied by heating the flow stream which heats the sample to the desired temperature. The experimental measurements were obtained for particle velocities ranging between 600 and 1200 ft/sec at temperatures ranging from ambient to 1500°F. Flat rectangular specimens were used in the tests. The erosion test specimens were 0.5 inch wide, 1 inch long and 0.25 inch thick, while the rebound test specimens were 0.25 inch wide. Test data were accumulated by setting the particle impingement angle at 15, 30, 45, 60 and 90 degrees for each of the different test temperatures and particle velocities.

RESTITUTION RATIO TEST RESULTS

The rebound dynamics of particles can be described in a statistical sense only. This becomes obvious when one examines the number of geometric situations that might occur at impact. After an incubation period, the target material will become pitted with craters, and in fact after a slightly longer period, a regular ripple pattern will form on the eroded surfaces. Thus, the local impact angle between the small particles and the eroded surface may deviate considerably from the geometric average. Also, the individual impact angle and velocity of a particle depend on its size. Furthermore, the particles themselves are irregular in shape, some with sharp corners. As the particle approaches the specimen, the orientation of the particle is, for the most part, random. Thus, some particles will impact on a flat surface and do very little work on the

target material. Others will impact with a corner oriented in a manner similar to that of a cutting tool and will remove material from the surface.

The restitution coefficient or restitution ratio is a measure of the kinetic energy exchange upon impact of two objects. Since the erosion is dependent on the erodent particle kinetic energy loss upon impacting the target, the restitution ratio will give a good indication of the type of the particle-material interaction. An erosive impact occurs when the contaminant particle is much harder than the target material. Therefore, the restitution ratio will be a measure of the distortion of the target material rather than distortion of the erosive particle.

Grant and Tabakoff [6] investigated thoroughly the rebound characteristics of high speed eroding particles. It was concluded that the restitution ratio V_2/V_1, which is directly related to the particle kinetic energy loss during an impact, does not give sufficient information in regard to erosion. Therefore, the restitution ratio was broken down into a normal velocity restitution ratio V_{N2}/V_{N1} (the normal component of the particle velocity after impact divided by the normal component of the particle velocity before impact), and a tangential velocity restitution ratio V_{T2}/V_{T1} (the tangential component of the particle velocity after impact divided by the tangential component of the particle velocity before impact) as shown in Fig. 4. The previous measurements at various incidence angles, temperature and flow velocities indicate that these ratios are mainly dependent upon the impingement angle for a given particle material combination [6].

In this investigation, the fly ash particle rebound conditions are measured using laser doppler velocimetry for particle laden flows over some of the sample materials listed in Tables 2 and 3. Figure 5 shows the fly ash particle size distribution, while Table 4 lists its chemical composition. The experimental results are presented in the form of tangential (V_{T2}/V_{T1}), normal (V_{N2}/V_{N1}), total velocity (V_2/V_1) and the directional (β_2/β_1) restitution ratios. Due to variations of the particle size and shape irregularities, the individual particle restitution ratios vary over a wide range. These variations are depicted in the restitution ratio histograms shown in Figs. 6 through 9. In these figures, the vertical axis represents the number of times that the restitution ratio was found to be between the limits designated by the scale at the horizontal axis. So

that the average of the measured impact velocities and angles have been used in restitution parameter calculations. The average of the particle impact velocities for the present investigation was 320 fps in all the particle restituion experiments.

Figures 10 through 13 present the results for M246 alloy with and without coatings, while Figures 14 through 17 present similar results for X40 alloy with and without coatings. Although the restitution ratios of M246 and X40 alloys had been reported in the last year, it has been rereported for completeness. The figures present the variation of the restitution ratios with the impact angle up to 90° range. The restitution ratios were assumed unity at 0° angle. The symbols in the Figures 10 through 17 represent the mean values of the experimentally measured restitution parameter at each impact angle. To facilitate the use of these experimental data in particle trajectory and erosion computations, empirical equations were obtained using a least square polynomial curve fit of the measured mean values of the restitution parameters. The curves in Figures 10 through 17 represent the polynomial curve fits and may be expressed by the following equations:

RT22

$$E_T = \frac{V_{T2}}{V_{T1}} = 1.0 + 8.164*10^{-4}\,\beta_1 - 5.981*10^{-4}\,\beta_1^2 + 1.2835*10^{-5}\,\beta_1^3 - 7.2016*10^{-8}\,\beta_1^4 \quad (1)$$

$$E_N = \frac{V_{N2}}{V_{N1}} = 1.0 - 0.025\,\beta_1 + 4.9815*10^{-4}\,\beta_1^2 - 3.5967*10^{-6}\,\beta_1^3 \quad (2)$$

$$E_V = \frac{V_2}{V_1} = 1.0 - 0.01386\,\beta_1 + 2.4201*10^{-4}\,\beta_1^2 - 2.0988*10^{-6}\,\beta_1^3 \quad (3)$$

$$E_\beta = \frac{\beta_2}{\beta_1} = 1.0 - 0.0175\,\beta_1 + 4.1312*10^{-4}\,\beta_1^2 - 2.9876*10^{-6}\,\beta_1^3 \quad (4)$$

RT22B

$$E_T = \frac{V_{T2}}{V_{T1}} = 1.0 - 0.0217\ \beta_1 + 4.0459*10^{-4}\ \beta_1^2 - 1.882*10^{-6}\ \beta_1^3 \quad (5)$$

$$E_N = \frac{V_{N2}}{V_{N1}} = 1.0 - 0.03624\ \beta_1 + 8.0027*10^{-4}\ \beta_1^2 - 5.5885*10^{-6}\ \beta_1^3 \quad (6)$$

$$E_V = \frac{V_2}{V_1} = 1.0 - 0.0233\ \beta_1 + 4.5889*10^{-4}\ \beta_1^2 - 3.3416*10^{-6}\ \beta_1^3 \quad (7)$$

$$E_\beta = \frac{\beta_2}{\beta_1} = 1.0 - 0.0117\ \beta_1 + 1.9963*10^{-4}\ \beta_1^2 - 1.3992*10^{-6}\ \beta_1^3 \quad (8)$$

RT44

$$E_T = \frac{V_{T2}}{V_{T1}} = 1.0 - 0.0195\ \beta_1 + 2.6855*10^{-4}\ \beta_1^2 - 4.2524*10^{-7}\ \beta_1^3 \quad (9)$$

$$E_N = \frac{V_{N2}}{V_{N1}} = 1.0 - 0.0389\ \beta_1 + 8.582*10^{-4}\ \beta_1^2 - 5.9095*10^{-6}\ \beta_1^3 \quad (10)$$

$$E_V = \frac{V_2}{V_1} = 1.0 - 0.027\ \beta_1 + 5.5878*10^{-4}\ \beta_1^2 - 4.0329*10^{-6}\ \beta_1^3 \quad (11)$$

$$E_\beta = \frac{\beta_2}{\beta_1} = 1.0 - 0.0195\ \beta_1 + 4.6328*10^{-4}\ \beta_1^2 - 3.2842*10^{-6}\ \beta_1^3 \quad (12)$$

RT44B

$$E_T = \frac{V_{T2}}{V_{T1}} = 1.0 - 0.0845\ \beta_1 - 6.2787*10^{-6}\ \beta_1^2 + 1.4787*10^{-6}\ \beta_1^3 \quad (13)$$

$$E_N = \frac{V_{N2}}{V_{N1}} = 1.0 - 0.0352\ \beta_1 + 7.3609*10^{-4}\ \beta_1^2 - 4.9794*10^{-6}\ \beta_1^3 \quad (14)$$

$$E_V = \frac{V_2}{V_1} = 1.0 - 0.0147\ \beta_1 + 1.9725*10^{-4}\ \beta_1^2 - 1.4659*10^{-6}\ \beta_1^3 \quad (15)$$

$$E_\beta = \frac{\beta_2}{\beta_1} = 1.0 - 0.0276\ \beta_1 + 6.7307*10^{-4}\ \beta_1^2 - 4.6255*10^{-6}\ \beta_1^3 \quad (16)$$

"C" Coating

$$\frac{V_{T2}}{V_{T1}} = e_T = 1.00 - 0.014949\ \beta_1 + 0.00011676\ \beta_1^2 + 3.27*10^{-7}\ \beta_1^3 \quad (17)$$

$$\frac{V_{N2}}{V_{N1}} = e_N = 1.00 - 0.0096558\ \beta_1 - 0.0006071*\beta_1^2 + 1.61091*10^{-5}\ \beta_1^3 - 1.04888*10^{-7}\ \beta_1^4 \quad (18)$$

$$\frac{V_2}{V_1} = e_V = 1.00 + 0.0024071\ \beta_1 - 0.000934\ \beta_1^2 + 1.89526 \times 10^{-5}\ \beta_1^3 - 1.11169 \times 10^{-7}\ \beta_1^4 \quad (19)$$

$$\frac{\beta_2}{\beta_1} = e_\beta = 1.00 - 0.001127\ \beta_1 - 0.0005889\ \beta_1^2 + 1.53245 \times 10^{-5}\ \beta_1^3 - 1.03 \times 10^{-7}\ \beta_1^4 \quad (20)$$

"N" Coating

$$\frac{V_{T2}}{V_{T1}} = e_T = 1.00 - 0.0124107\ \beta_1 + 2.97165*10^{-5}\ \beta_1^2 + 9.35159*10^{-7}\ \beta_1^3 \quad (21)$$

$$\frac{V_{N2}}{V_{N1}} = e_N = 1.00 + 0.00275521\ \beta_1 - 0.0012869\ \beta_1^2 + 2.72264*10^{-5}\ \beta_1^3 - 1.604*10^{-7}\ \beta_1^4 \quad (22)$$

$$\frac{V_2}{V_1} = e_V = 1.00 + 0.0037812\ \beta_1 - 0.000977626\ \beta_1^2 + 1.94275 \times 10^{-5}\ \beta_1^3 - 1.12*10^{-7}\ \beta_1^4 \quad (23)$$

$$\frac{\beta_2}{\beta_1} = e_\beta = 1.00 - 0.000159243\ \beta_1 - 0.000723929\ \beta_1^2 + 1.81865*10^{-5}\ \beta_1^3 - 1.185*10^{-7}\ \beta_1^4 \quad (24)$$

For M-246 Alloy

$$\frac{V_{T2}}{V_{T1}} = e_T = 1.00 - 0.00832249\ \beta_1 - 8.09523*10^{-5}\ \beta_1^2 + 1.78601*10^{-6}\ \beta_1^3 \quad (25)$$

$$\frac{V_{N2}}{V_{N1}} = e_N = 1.00 + 0.00809841\ \beta_1 - 0.00122611\ \beta_1^2 + 2.30864*10^{-5}\ \beta_1^3 - 1.2922*10^{-7}\ \beta_1^4 \quad (26)$$

$$\frac{V_2}{V_1} = e_V = 1.00 + 0.00601123\ \beta_1 - 0.000957896\ \beta_1^2 + 1.77426*10^{-5}\ \beta_1^3 - 9.94*10^{-8}\ \beta_1^4 \quad (27)$$

$$\frac{\beta_2}{\beta_1} = e_\beta = 1.00 + 0.00872424\ \beta_1 - 0.000834276\ \beta_1^2 + 1.63771*10^{-5}\ \beta_1^3 - 9.75683*10^{-8}\ \beta_1^4 \quad (28)$$

X-40 Alloy

$$\frac{V_{T2}}{V_{T1}} = e_T = 1.00 - 0.0110425\ \beta_1 + 2.38155*10^{-5}\beta_1^2 + 9.38784*10^{-7}\ \beta_1^3 \quad (29)$$

$$\frac{V_{N2}}{V_{N1}} = e_N = 1.00 - 0.00393812\ \beta_1 - 0.0007443\ \beta_1^2 + 1.66937*10^{-5}\ \beta_4^3 - 1.01213*10^{-7}\ \beta_1^4 \quad (30)$$

$$\frac{V_2}{V_1} = e_V = 1.00 + 0.000951\ \beta_1 - 0.00725\ \beta_1^2 + 1.43015*10^{-5}\ \beta_1^3 - 8.34*10^{-8}\ \beta_1^4 \quad (31)$$

$$\frac{\beta_2}{\beta_1} = e_\beta = 1.00 + 0.001295\ \beta_1 - 0.000645\ \beta_1^2 + 1.55053*10^{-5}\ \beta_1^3 - 1.008*10^{-7}\ \beta_1^4 \quad (32)$$

where β_1 is measured in degrees.

THEORETICAL MODEL OF SOLID PARTICLE IMPACT ON A TARGET OF DUCTILE MATERIAL

Introduction

The problem of describing solid particle impacts which cause erosion is very complex one and has not yet been solved completely. Theoretical codes based on the numerical solutions of the particle dynamic equation have been proposed. They have been used in analyzing rebound characteristics of materials which can be considered to behave in a ductile manner. Hutchings et al. [7] developed a computer model of oblique impact of a rigid sphere against rigid-plastic solid. They used it to predict the variation of rebound velocity and rebound angle with both impact angle and impact velocity for 9.5 mm diameter hard steel sphere impacting a mild steel target. The model underestimated the angle of rebound and failed to predict rebound velocity at normal impact. Sriram and Kosel [8] extended Hutchings et al. [9] model to include the elastic energy stored in the target, and the rotational energy of the particle. The model also employed a flow stress rather than friction force. The model overestimated the rebound velocity for high impact angles and predict a weak relationship between rebound angle and velocity. The numerical solution main difficulties occur because of the unknown conditions of the materials during impact which necessitates that some assumptions must be made. A completely different approach has been employed in the present investigation to analyze solid particle impact on a ductile material target.

Theoretical Formulation

A theoretical model of a single solid particle impact on the target of ductile materials has been developed based on the elastic-plastic theory and Rankine-Hugoniot relation for pressure correlations in the plastic region. The effect of strain rate on the strength of material is also included in this model. It has been assumed that the impacted target and particle behave like time varied elastic-plastic bodies under the influence of strain rate. Due to the ductility of the investigated materials, the fracture mechanism is not included in this model. The constitutive equations and the equations of motion are solved independently. Lagrangian formulations of conservation of mass,

momentum and energy have been employed to provide the geometrical distortions of target and particle. The yield condition, which depends on the strain rate and strain energy, is used to define the interface of elastic and plastic flows in the materials.

The Governing Equations:

The governing equations written in two dimensional Cartesian coordinates are:

Equation of Motion:

$$\rho_t \frac{\partial \dot{x}}{\partial t} = \frac{\partial \Sigma_{xx}}{\partial x} + \frac{\partial \tau_{xy}}{\partial y} \quad , \tag{33}$$

$$\rho_t \frac{\partial \dot{y}}{\partial t} = \frac{\partial \Sigma_{yy}}{\partial y} + \frac{\partial \tau_{xy}}{\partial x} \tag{34}$$

where

$$\Sigma_{xx} = S_{xx} - (P+q) \ ,$$
$$\Sigma_{yy} = S_{yy} - (P + q) \tag{35}$$

Continuity Equation

$$\frac{\dot{V}}{V} = \frac{\partial \dot{x}}{\partial x} + \frac{\partial \dot{y}}{\partial y} \tag{36}$$

$$= \dot{\epsilon}_{xx} + \dot{\epsilon}_{yy}$$

where velocity strains are defined as:

$$\dot{\epsilon}_{xx} = \frac{\partial \dot{x}}{\partial x} \quad , \qquad \dot{\epsilon}_{yy} = \frac{\partial \dot{y}}{\partial y} \tag{37}$$

Energy Equation

$$\dot{E} = -(P + q)\,\dot{V} + V\,(S_{xx}\,\dot{\epsilon}_{xx} + S_{yy}\,\dot{\epsilon}_{yy} + \tau_{xy}\,\dot{\epsilon}_{xy}) \tag{38}$$

where velocity strain, $\dot{\epsilon}_{xy}$, is defined as:

$$\dot{\epsilon}_{xy} = \frac{\partial \dot{y}}{\partial x} + \frac{\partial \dot{x}}{\partial y} \quad . \tag{39}$$

Equations of State:

$$\dot{S}_{ii} = 2\mu\,(\dot{\epsilon}_{ii} - \frac{1}{3}\,\frac{\dot{V}}{V}) + \delta_{ii} \quad , \tag{40}$$

$$\dot{\tau}_{xy} = \mu(\dot{\epsilon}_{xy}) + \delta_{xy} \tag{41}$$

where subscript ii represent the subscripts xx, yy or zz.

Hydrostatic Pressure:

In the elastic limit, hydrostatic pressure has been expressed as follows:

$$P = -(\lambda + \mu)\,\ell n\,V \quad , \tag{42}$$

where λ and μ are Lame constants.

Beyond the elastic limit, empirical Hugoniot formulation is used:

$$P = a(\eta - 1) + b(\eta - 1)^2 + c(\eta - 1)^3 \tag{43}$$

where $\eta = \frac{1}{V} = \frac{\rho}{\rho_0}$,

a, b and c are constants.

Artificial Viscosity:

In the above equations the artificial viscosity "q" has been expressed as follows:

$$q = C_0^2\,\rho_0\,(\frac{\dot{V}}{V})^2\,\frac{A}{V} \tag{44}$$

where $C_0 = 2$.

Von Mises Yield Condition:

$$S_1^2 + S_2^2 + S_3^2 - \frac{2}{3} Y_0^2 \leq 0 \tag{45}$$

where Y_0 is the yield strength.

For consistency with simple tension tests, when tension occurs in the material, the pressure is cut off at:

$$P = -\frac{1}{3} Y_0 . \tag{46}$$

The expression for deviatoric stresses are modified to include small correction terms "δ" for body rotation.

A semi-empirical formulation [10, 11] of yield strength for steel is used in the numerical calculations.

The Numerical Method

A numerical scheme has been developed using the finite volume technique with arbitrary mesh configuration. This scheme is consistent, second order accurate in time and first order accurate in space. For a better unsteady resolution, the two step explicit MacCormack algorithm is applied to the governing equations.

Predictor:

$$U^{*n+1}_{i,j} = U^n_{i,j} - \Delta t \, A^n \tag{47}$$

Corrector:

$$U^{n+1}_{i,j} = U^n_{i,j} - \Delta t \, (A^{N+1} + A^n) \tag{48}$$

A^{n+1} is calculated from U^{*n+1}, where U can be replaced by $\dot{x}$ or $\dot{y}$. The operator A is derived from the finite volume integration around a quadrilateral or triangular mesh.

Results and Discussion

The numerical solution has been obtained for 9.5 mm diameter hard tool steel cylindrical particle impacting 5 cm wide x 3 cm thickness mild steel target. The mesh used in the numerical simulation consists of a 151x31 target grid and a 39x8 particle grid. Besides the stress and strain distributions through both the target and particle, the numerical solution provides particle rebound velocity, particle rebound angle and particle kinetic energy loss for a wide range of particle impact angles and velocities. Figures 18 through 20 present the variation of rebound velocity, rebound angle and particle kinetic energy loss with the impact velocity for impact angle ranging from 20° to 90°. Inspection of Figs. 18 and 20 shows that the predicted particle rebound velocity and kinetic energy loss satisfactorily agree with the experimental data obtained by Hutchings et al. [9]. Similar satisfactory results can be observed in Fig. 19 for impact angle up to 45°. The present results have shown that the newly developed theory incorporated in the particle impact code can predict the rebound characteristics for both normal and oblique impacts. With more accurate empirical model for strain rate, strain hardening and adiabatic shear band the prediction will be much better.

EROSION TEST RESULTS

The erosion tests were conducted to obtain the erosion rate for alloys and coatings listed in Tables 2 and 3. The erosion rate is defined as the ratio between the change in the sample mass and the mass of the impacting particles. In each test, the specimen was impacted by a pre-weighed dose of particles. After each particle dose had impacted the sample, its surface was cleaned, the specimen was weighed, and the change in specimen weight was recorded. The erosion rate was determined from the relation:

$$\text{erosion rate} = \frac{\text{change in mass of sample}}{\text{mass of impacting particles}} \quad . \tag{49}$$

The experimental results show the effect of the main erosion parameters, namely, impact velocity, impact angle and sample temperature on the material erosion rate. The erosion test results had been presented in the previous final report for IN-738, FSX-414, M246 and X40 alloys and C, N, RT22, RT22B, RT44, RT44B and chromium carbide coatings. These superalloys and coatings are widely used in gas turbine components. In the present investigation, the erosion behavior of coatings and alloys intended for steam turbine component have been studied. The experimental data for 410 stainless steel and LC1-1B, LC-1H, SDG-2207 and plasma spray coatings have been presented in this final report. Since the solid particles in steam turbines are mainly boiler scales, chromite particles have been used in the present investigation. The chromite particle chemical analysis is listed in Table 5, while figure 21 shows its size distribution.

Impingement Angle Effect on the Erosion Rate

It is well known that erosion rate is a function of particle impingement angale. For a ductile material, erosion rate increases from zero at 0° particle impact angle to a maximum as impact angle is increased. After reaching a maximum, the erosion rate decreases to a minimum value at 90°. On the other hand, erosion rate of a brittle material increases from zero at 0° impact angle to a maximum value at 90°.

410 Stainless Steel:

AISI Type 410 is a hardenable 12% chromium stainless steel. It offers a wide range of mechanical properties and has good resistance to corrosion and oxidation. Among its many applications are steam turbine components. Therefore, it has been included in the test program.

The variation of 410 stainless steel erosion rate with impingement angle is shown in Fig. 22 for two velocities. The figure indicates that 410 stainless steel has ductile erosion behavior with maximum erosion rate at 25° impact angle. This figure, also, illustrates qualitatively the strong effect of particle impact velocity on the erosion rate.

LC-1B Coating:

It is a detonation gun coating containing about 65% chromium carbide, the balance being 80 Ni/20 Cr alloy (nichrome). The nichrome powder size was 44μ fraction. It has developed for steam turbine components. The impingement angle effect on the erosion rate of LC-1B coating exhibits a brittle erosion pattern with maximum erosion rate at 90° as shown in Fig. 23. Initially the erosion rate increases rapidly with impingement angle increase reaching maximum in the 30°-45° range of impingement angle after which it remains approximately constant.

LC-1H Coating:

LC-1H is a detonation gun coating containing 80% chromium carbide, of Cr_7C_3 composition, and 20% nichrome. The nichrome powder used for LC-1H is of finer size than the powder used for LC-1B, being a 20μ fraction. This coating was developed for steam turbines. Figure 24 presents the variation of LC-1H erosion rate with impingement angle. The erosion rate reaches the maximum value at 90° which indicates the brittle nature of LC-1H coating. Inspection of Figs. 23 and 24 reveals that LC-1H coating has better erosion resistance than LC-1B coating at both test velocities. The superiority of LC-1H over LC-1B, which employs powders mixed in the same ratio, is attributed to the finer particle size powders (20μ) used for LC-1H. In the range of 45°-90° impingement angle, LC-1H shows small increase in the erosion rate with increasing impingement angle.

Plasma Spray Coating:

It is a plasma deposit of 85% Cr_3C_2 and 15% FeCrAlY powder. This coating was given a 72 hours exposure at 1022°F before testing. The erosion test results show continuous increase of plasma coating erosion rate with increasing impingement angle as shown in Fig. 25. The figure indicates that the erosion rate curves follow the familiar form of brittle erosion with maximum at 90°. The velocity effect on the erosion rate can be clearly observed in Fig. 25.

SDG-2207 Coating:

SDG-2207 is a super D-Gun coating made from a powder mix containing 89% Cr_3C_2 and 11% inconel 718 powder. The influence of the impingement angle on the erosion rate of SDG-2207 coating is presented in Fig. 26 for 750 and 1000 fps particle impact velocity. The figure illustrates that the coating exhibits brittle erosion pattern with maximum erosion at 90°. The erosion rate shows small variation with impingement angle in 45°-90° range.

Comparison Between 410 Stainless Steel and Coatings Erosion Rates

Figures 27 and 28 present erosion rates for 410 stainless steel, LC-1B, LC-1H, SDG-2207 and plasma coatings at oblique (30°) and normal (90°) impact angles for 750 and 1000 fps impact velocities. At small impact angle ($\leq$30°), the tested coatings showed better erosion resistance than 410 stainless steel. Therefore, at small impact angles, these coatings provide good erosion resistance and prolong the life of the steam turbine components, significantly. SDG-2207 coating, whose erosion rate is one half the erosion rate of 410 stainless steel, offers the best erosion resistance at 30° impact angle and 750 fps impact velocity as shown in Fig. 27. However at impact velocity of 1000 fps, LC-1H coatings exhibits the lowest erosion rates (40% less than 410 stainless steel erosion rate) compared to the other coatings.

At large impact angles (>35°),a the coatings erosion rates were much higher than stainless steel erosion rate due to the coating brittleness. Figure 28 indicates that the 410 stainless steel erosion rate is less than one third the erosion rate of the best coating (SDG-2207) at 90°.

Velocity Effect on Erosion Rates

The influence of particle impact velocity on 410 stainless steel and coatings are shown in Figs. 29 through 33 for different impact angles at sample temperature of 1022°F. In these figures, the solid lines represent power law curve fit of the experimental data at each angle. The velocity exponent, n, obtained by curve fitting is listed in the figures for each impingement angle. For 410 stainless steel the velocity exponent varies from 1.55 to 2.25 (Fig. 29). Figure 30 shows that LC-1B erosion rate is proportional to particle impact velocity to power ranging from 3.53 to 2.19. Velocity exponent obtained for LC-1H coating is in the vicinity of 2 (Fig. 31). While plasma spray coating shows vleocity exponent less than 2 (n = 1.32 - 1.87). Figure 33 reveals that SDG-2207 coating has a velocity exponent about 2.5. The different values of velocity exponent for different coatings for the same test conditions indicate the material properties effect on the erosion behavior. The variation of the exponent, n, for each coating reveals that n is dependent on the impact angle. The strong effect of the velocity on the material erosion rate is manifested by the high value of the velocity exponent.

Temperature Effect on the Erosion Rate:

To study the temperature effect on erosion rates, the investigated materials have been tested at ambient, 500°F and 1022°F sample temperature for partiacle velocity of 750 fps and maximum erosion angles (90° for coatings and 30° for 410 stainless steel). The experimental results are presented in Fig. 34. This figure shows that the temperature has similar effect on the tested coatings. The coating erosion rates continuously increase with increasing temperature. 410 stainless steel shows weak temperature effect in the testing temperature range. Increasing the temperature from 70°F to 1022°F, doubled the erosion rate of SDG-2207 coating, and increases the erosion rate of the other coatings by 20% as it can be observed in Fig. 34.

DUCTILE EROSION RATE MODEL

For analyzing material erosion by solid particles, the material behavior has idealized as either "ductile" or "brittle" to enable solutions to be developed. An ideally brittle material fractures after only plastic deformation, while ideally ductile material undergoes very large plastics strains before material removal. For ductile material erosion, further simplifications have been made by assuming two erosion mechanisms: one at low impingement angle and another at normal impact. At intermediate impingement angle, a combination of the two mechanisms was proposed. Following this approach, erosion models have been proposed for ductile erosion at oblique and normal impact.

Erosion Model at Low Impingement Angle

Several mechanisms have been proposed for a ductile material erosion at oblique impact. Cutting [12, 13], ploughing [14, 15] and platelet [16] mechanisms are some of the described mechanisms. Generally in the erosion process, the material removal depends on the crater volume formed by the particle. The crater volume depends on the maximum particle penetration normal to the surface and also on the particle displacement parallel to the surface. Since the crater shape is not critical parameter in material erosion, its geometry can be simplified. The simplified crater depth can be assumed constant. Although the proposed and actual crater shapes are different, their volumes are assumed equal.

The normal penetration is a plastic deformation which depends on the normal force exerted by the particle upon impacting the target. This normal force depends on the change of momentum between the particle and the surface in the normal direction upon impact. The tangential displacement depends on the energy required to remove (or deform) the target material tangentially. This energy depends on the exchange of tangential kinetic energy between the particle and target upon impact.

Considering a modified crater shape, the erosion process can be described in two steps as depicted in Fig. 35. First the particle penetrates the surface normally, then moves tangentially parallel to the undisturbed surface removing target material.

This simplified description of the erosion process is similar to the machining where the tool is normally fed to a certain depth into the specimen, then tangential removal of the material occurs by tool-specimen relative movement.

Based on the above discussion, the crater depth ,h, depends on the force exerted by the particle which is proportional to the particle momentum in the normal direction; i.e.:

$$h \propto M_P \, V_{N1} \tag{50}$$

where h: an average crater depth,

M_P: particle mass,

V_{N1}: normal component of the particle impact velocity.

The tangential particle displacement depends on the energy required for material removal which is proportional to kinetic energy exchange between the particle and the target tangentially upon impact.

$$D_T \propto M_P \, (V_{T1}^2 - V_{T2}^2)$$

$$\propto M_P \, V_{T1}^2 \, [1 - (\frac{V_{T2}^2}{V_{T1}^2})] \tag{51}$$

where D_T: an average particle displacement in the tangential direction,

V_{T1}: tangential component of particle impact velocity,

V_{T2}: tangential component of particle rebound velocity.

Since, tangential restitution ratio, E_T, is defined as

$$E_T = \frac{V_{T2}}{V_{T1}} \tag{52}$$

Equation (51) can be written in the following form:

$$D_T \propto M_P \, V_{T1}^2 \, (1 - E_T^2) \tag{53}$$

The volume of the material removed, Vol., depends on the depth, h, and displacement, D_T, i.e.

$$Vol \propto h \times D_T \tag{54}$$

where Vol: crater volume,

V_1: particle impact velocity,

β_1: particle impingement angle.

Using Eqs. (50) and (53), equation (54) can be written as:

$$\begin{aligned} Vol &\propto M_P V_{N1} \times M_P V_{T1}^2 (1 - E_T^2) \\ &\propto M_P^2 V_1^3 \sin\beta_1 \cos^2\beta_1 (1 - E_T^2) \end{aligned} \tag{55}$$

Consequently, material weight loss can be expressed as follows:

$$\begin{aligned} \Delta W &= \rho_t Vol \\ &= C_0 M_P^2 V_1^3 \sin\beta_1 \cos^2\beta_1 (1 - E_T^2) \end{aligned} \tag{56}$$

where C_0 : a constant depends on the target material,

ΔW : material weight loss,

ρ_t : material density.

Dividing Eq. (56) by the particle mass, M_P, the erosion mass rate can be expressed as follows:

$$\epsilon_c = C_0 M_P V_1^3 \sin\beta_1 \cos^2\beta_1 (1 - E_T^2) \tag{57}$$

where ϵ_c: material erosion per unit mass of particles. Since the particle mass can be assumed constant, equation (57) can be written as follows:

$$\epsilon_c = C_{11} V_1^3 \sin\beta_1 \cos^2\beta_1 (1 - E_T^2) \tag{58}$$

where C_{11}: constant,

$$= C_0 M_P$$

The above expression of the material erosion rate indicates that the velocity exponent is three. This value of the velocity exponent agree better with the most velocity exponent values obtained experimentally. Equation (58) is similar to the hypothetical erosion model proposed by Grant [6] with different velocity exponents and $f(\beta) = \sin\beta$.

Erosion Model at Normal Impact

Though much experimental information has been obtained on normal impact erosion, the basic mechanism are not yet agreed upon. The mechanism of ductile erosion at normal impact can not be described by machining or scratching or ploughing mechanisms. Finnie [17] proposed hypothetically that ductile erosion at normal impact can result from multiple impact, battering the surface back and forth, produce fracture by low- cycle fatigue. The surface deformation due to multiple impact has been observed also by Levy [16].

The amount of material plastic deformation depends on the kinetic energy exchange between the particle and the target at normal impact. So that it has been assumed in this analysis that material erosion is proportional to change of particle normal velocity kinetic energy. Therefore, the material erosion has been proposed as follows:

$$\Delta W_{90} = C_{22} M_P (V_{N1}^2 - V_{N2}^2)$$

$$= C_{22} M_P V_{N1}^2 \left(1 - \frac{V_{N2}^2}{V_{N1}^2}\right) \qquad (59)$$

where ΔW_{90}: material removal at normal impacts,

V_{N1} : normal component of particle impact velocity,

V_{N2} : normal component of particle rebound velocity,

C_{22} : empirical constant .

Defining normal restitution ratio, E_N, as:

$$E_N = \frac{V_{N2}}{V_{N1}} \tag{60}$$

and dividing by particle mass, the material mass erosion can be express as follows:

$$\epsilon_{90} = C_{22}\, V_{N1}^2\, (1 - E_N^2)$$
$$= C_{22}\, V_1^2 \sin^2\beta_1\, (1 - E_N^2) \tag{61}$$

where ϵ_{90} : mass erosion per unit mass of particles at 90°.

Prediction of the Superalloy and Coating Erosion Rates

The total material erosion has been calculated at any angle by superimposing the two type of erosion described by Eqs. (58) and (61). The general relationship of the total erosion can be expressed as follows:

$$\bar{\epsilon} = \epsilon_c + \epsilon_{90}$$
$$= C_{11}\, V_1^3 \sin\beta_1 \cos^2\beta_1\, (1 - E_T^2) + C_{22}\, V_1^2 \sin^2\beta_1 (1 - E_N^2) \tag{62}$$

where $\bar{\epsilon}$: total mass erosion per unit mass of particles.

Although the experimental results showed that the velocity exponent is in the vicinity of three, the measured values were different for different materials. Some of the tested materials show velocity exponent higher than the predicted values and other show lower values. This might due to the effect of the other parameters effecting on the erosion rate which are not modeled in this analysis. Therefore the total mass erosion rate (Eq. (62)) has been modified to the following form.

$$\bar{\epsilon} = C_{11}\, V_1^{n1} \sin^{n2}\beta_1\, (1 - E_T^2) + C_{22}\, V_1^{n4} \sin^2\beta_1\, (1 - E_N^2) \tag{63}$$

where the exact values of the exponent are empirically determined. In addition the erosion rate has been found to vary with target temperature. In this

study, erosion rate was observed to change slightly with varying target temperature for most of the investigated materials. However, when the target temperature approached the level at which the yield strength begins to drop rapidly, the erosion rate increases abruptly. Therefore, the same approach used by Wakeman [18] has been employed to corporate the temperature effect on the erosion rate by using an empirical expression to match the data as follows:

$$\bar{\epsilon} = F(T)\ \bar{\epsilon}_{RT} \tag{64}$$

where:

$$F(T) = \left(\frac{Y_{RT}}{Y}\right)^{a} + \frac{Y}{Y_{RT}} - 1 \tag{65}$$

where $\bar{\epsilon}$: erosion rate at operating temperature,

$\bar{\epsilon}_{RT}$: erosion rate at reference temperature,

Y : material yield strength at operating temperature,

Y_{RT} : material yield strength at reference temperature,

a : empirical constant.

The ambient temperature has been taken as a reference temperature. Therefore, F(T) at ambient is equal to one and the erosion rate at ambient temperature can be expressed by Eq. (63).

Combining Eqs. (63), (64), and (65) gives:

$$\epsilon = F(T)\ [C_{11}(V_1/100)^{n1} \sin^{n2}\beta_1 \cos^{n3}\beta_1\ (1 - E_T^2) + C_{22}(V_1/100)^{n4} \sin^{2}\beta_1 (1 - E_N^2)] \tag{66}$$

where ϵ: erosion rate, mgm/gm

V: impact velocity, m/s

β: impact angle, rad.

The erosion rate model as described above gives the erosion rate as a function of material yield strength, particle impact velocity, impingement angle and particle velocity restitution ratios. The restitution ratios have been calculated using the equations developed earlier. The constants C_{11}, and C_{22}

and the exponents, n's, are determined empirically from the experimental data by using multiple regression analysis. The term $(V_1/100)$ is used in place of V_1 to control the magnitude of C_{11} and C_{22} in the correlation. Table 6 summarizes the values of the constants and exponents for the investigated alloys and coatings whose erosion behaviors are ductile.

Using the semi-empirical equations the erosion rates (mgm/gm) have been calculated for the investigated superalloys and coatings for different velocities (m/s), impingement angles and temperatures. Figures 36 through 39 represent predicted erosion rates against measured erosion rates for INCO-738, FSX-414, M246 and X40 alloys. The material yield strength for the superalloys have been substituted into the temperature parameters, F(T). These terms have been plotted against target temperature in Fig. 40 for each material. The temperature parameters value have been used in the calculations involved with the erosion rate equations. Figures 41 through 43 show comparison between calculated and measured erosion rates for N, RT22 and RT22B coatings. Due to lack of information about coatings yield strength, it was not possible to calculate its temperature parameters. The figures show that the calculated erosion rates correlate well with measured erosion rates.

PARTICLE TRAJECTORIES AND BLADE EROSION IN A TWO-STAGE TURBINE BASED ON REBOUND AND EROSION MODELS

The proposed rebound and erosion models have been used to predict particle trajectories and blade erosion in a two stage axial flow gas turbine. The investigation involved three major modeling efforts, namely, (i) modeling the three dimensional flow field in each blade row, (ii) prediction of the three dimensional particle dynamics under the influence of the flow field aerodynamic forces and the interactions with blades, hub and shroud, and (iii) blade erosion computation based on particle impact data and erosion model of the blade material.

Particle Trajectories

Due to their higher inertia, the particle trajectories in turbomachines generally differ from the flow streamlines and particles tends to impact the blade surfaces and hub and tip walls. In addition, the particles migrate radially under the influence of centrifugal forces as they acquire circumferential velocities either through blade surface impacts or under the influence of the flow field. Therefore, accurate particle-surface impact modeling is accential for particle trajectory computations.

The particle trajectory calculation consists of numerical integration of the particle three dimensional equations of motion in the flow field, up to the point of blade, hub or casing impact. The magnitude and direction of particle rebound velocity after these impacts are predicted by using rebound model developed for the particle-material combination under consideration. Such computations have been conductred based on the proposed rebound model to investigate the trajectories in the flow passages of a two stage turbine for fly ash particles with different diameters. The detailed description of computation technique and results can be found in Ref. [19] which has won the best paper award.

Figure 44 shows samples of particle trajectories projected in θ-z plane for four selected particle diameters of 2.5, 15, 40 and 135 microns. The figureS clearly indicate that the particle deviation from the streamlines increases as the particle diameter increases due to increase of particle inertia. So that most of the large particles tend to impact the pressure

side of the first stator and some impacts the leading edges, while small particles follow the flow streamlines with a few or no impacts (Fig. 44a). At the first stator exit, the large particle absolute velocities are much lower than the gas velocity. Therefore, they enter the first rotor with very high negative incidence angles which causes the large particles to impact the blae suction surface near the rotor leading edge. After rebounding, they impact the rotor blade pressure surface near the trailing edge. In the second stage, similar behaviors can be observed for the small and large particles.

The projection of particle trajectories in r-z plane is shown in Fig. 45 for the different particle diameters. The results demonstrate the strong influence of blade impacts on the large particles, which are centrifuged towards the tip after the blade impacts. This leads to high particle concentrations near the blade tips resulting in higher erosion damages at tip.

Particle trajectory computations provide, also, particle impact location coordinates, the impact velocity magnitude, and impingement angle relative to the blade surface at each impact location. Figure 46 shows impact locations for 15 microns particles in a two stage turbine over the blade pressure surfaces. The effect of particle centrifugation are noticeable in the absence of impacts near the blade hubs. The particle size effect on the blade impacts is illustrated in Fig. 47. This figure represents the impact location over the first rotor pressure surface for different particle diameters. Figure 47 shows that particle migration towards the tip increases with increase of particle diameter which leads to increased particle impacts towards the blade tips.

Blade Surface Erosion

The prediction of turbine blade erosion is based on the particle impact data as determined from the trajectories and erosion model developed for the particle-material combination. Based on the erosion models developed for M246 alloy and N and RT22 coating, the blade surface erosion have been predicted in a two stage turbine. The results are recently presented in the 5th International Symposium and Exposition on Gas Turbines in Cogeneration, Repowering and Peak-Load Power Generation in Budapest, 1991 [20]. Some of

these results are shown in Figs. 48 through 51. These figures present the spacial distribution of the erosion parameter (material weight loss per unit mass of particles per unit surface area) over the blade pressure surfaces in the two stage turbine for uncoated (M246 alloy) and coated surfaces (N and RT22 coatings). Although the coatings did not change the erosion pattern significantly over the blade surfaces, they remarkably reduced the blade erosion. Comparing the values of maximum erosion at the mid span of the trailing edge (Fig. 48) reveals that the uncoated blade maximum erosion is one order of magnitude the maximum erosion of coated blade. Figure 49 shows that the reduction of the maximum erosion at the rotor tip leading edge is 70% for N coating and 95% for RT22 coating. This strong influence of the blade coating on the erosion can be clearly seen in Fig. 50 and 51 which show the erosion parameter of the second stage. This remarkable improvement of coated surface erosion prolongs greatly the blade life and reduces the blade material degradation due to particulated flows.

REFERENCES

1. Tabakoff, W. and Wakeman, T., "Test Facility for Material Erosion at High Temperature," ASTM Special Publication 664, 1979, pp. 123-135.

2. Tabakoff, W., Hamed, A. and Eroglu, H., "Study of Particles Rebound Characteristics and Material Erosion at High Temperature," Final Technical Report, Fossil Energy Materials Program, U.S. Department of Energy, ORNL/Sub/84-89628/01, December 1986.

3. Tabakoff, W. and Hamed, A., "Laser Measurements of Solid Particles Rebound Parameters Impacting on 2024 Aluminum and 6Al-4V Titanium Alloys," AIAA Journal of Aeronautics and Astronautics, Vol. 25, May 1987, pp. 721-726.

4. "Aerospace Structural Metals Handbook", Syracuse University Press, 1963.

5. Alloy Digest, Engineering Alloy Digest Inc., Upper Montclair, N.J., 1969.

6. G. Grant and W. Tabakoff, "Erosion Prediction in Turbomachinery Resulting from Environmental Solid Particles," Journal of Aircraft, Vol. 12, No. 5, May 1975, pp 471-478.

7. Hutchings, I.M., Winter, R.E. and Field, J.E., "Solid Particle Erosion of Metals: The Removal of Surface Material by Spherical Projectiles," Proc. R. Soc. Lond. A. 348, 1976, pp. 379-392.

8. Sriram, T.S. and Kosel, T.H., "Computer Modeling of the Rebound Characteristics of Spherical Erodent Particles," Proc. of the 7th Int. Conf. on Erosion by Liquid and Solid Impact, Cambridge, September 6-10, 1987, Cambridge.

9. Hutchings, I.M., Rickerby, D.G. and Macmillan, N.H., "Further Studies of the Oblique Impact of a Hard Sphere Against a Ductile Solid," Int. J. Mech. Sci., Vol. 23, 1981, pp. 639-646.

10. Rosefield, A.R. and Hahn, G.T., "Numerical Descriptions of the Ambient Low-Temperature and High-Strain Rate Flow and Fracture Behavior of Plain Carbon Steel," Trans. of the ASME, Vol. 59, pp. 962-982, 1966.

11. Wilkins, Mark L., "Calculation of Elastic-Plastic Flow," Method in Computational Physics, Vol. 3, PP 211-263, 1964.

12. Finnie, I., "An Experimental Study of Erosion," Proc. of the Soc. of Experimental Stress Analysis, Vol. 17, No. 2, 1959, pp. 65-70.

13. Winter, R.E. and Hutchings, I.M., "Solid Partiacle Erosion Studies Using Single Angular Particles," Wear, Vol. 29, 1974, pp. 181-194.

14. Hutchings, I.M. and Winter, R.E., "Particle Erosion of Ductile Metals: A Mechanism of Material Removal," Wear, Vol. 27, 1974, pp. 121-128.

15. Hutchings, I.M., Winter, R.E., and Field, J.E., "Solid Particle Erosion of Metals: The Removal of Surface Material by Spherical Projectile," Proc. Roy. Soc., London A, vol. 348, 1976, pp. 379-392.

16. Levy, A., "The Platelet Mechanism of Erosion of Ductile Metals," Wear, Vol. 108, 1986, pp. 1-21.

17. Finnie, I., "Some Observations on the Erosion of Ductile Metals," Wear, Vol. 19, 1972, pp. 81-90.

18. Wakeman, T., "Erosion Predictions and Measurements in High Temperature Particulate Flow Environments," Ph.D. Dissertation, Department of Aerospace Engineering and Engineering Mechanics, University of Cincinnati, 1982.

19. Tabakoff, W., Hamed, A. and Metwally, M., "Effect of Particle Size Distribution on Particle Dynamics and Blade Erosion in Axial Flow Turbines," ASME Paper No. 90-GT-114.

20. Tabakoff, W. and Metwally, M., "Coating Effect on Particle Trajectories and Turbine Blade Erosion," 5th International Symposium and Exposition on Gas Turbines in Cogeneration, Repowering and Peak-Load Power Generation, Budapest, September 3-5, 1991.

Table 1: LDV Characteristics

	Purple	Blue	Green
Wave length λ (μm)	0.4765	0.488	0.5145
Fringe spacing λ (μm)	2.784	2.851	3.0
Diameter of measuring vol (mm) at e^{-2} intensity location	0.052	0.053	0.056
Length of measuring vol (mm)	0.603	0.617	0.651
No. of stationary fringes	19	19	19

Table 2 - Tested Superalloys

Superalloy	Chemical Composition
INCO IN-738	16 Cr, 8.5 Co, 3.4 Al, 3.4 Ti, 2.6 W, 1.75 Mo, 1.75 Ta, 0.9 Cb, balance Ni
MAR-M246	10 Co, 10 W, 9 Cr, 5.5 Al, 2.4 Mo, 1.5 Ta, 1.5 Ti, balance Ni
X40	25 Cr, 10 Ni, 7.5 W, balance Co
FSX-414	29.5 Cr, 10.5 Ni, 7W, 2 Fe, balance Co
AISI 410	12 Cr, 1 Mg, 1 Si, balance Fe

Table 3 - The Tested Coatings

Coating	Treatment	Substrate	Thickness (mils)	Heat Treatment
C	Aluminized	X40*	3	--
N	Aluminized	M246**	3	--
RT22	Platinum Aluminized	M246	5	yes
RT228	Rhodium/Platinum Aluminized	M246	3	yes
RT44	Low Rhodium/Platinum Aluminized	X40	3	no
RT44B	Rhodium/Platinum Aluminized	X40	3	no
Chromium-Carbide	Chromized	INCO 718	5	--
LC-1B	--	INCO 718	200	yes
LC-1H	--	INCO 718	200	yes
SDG-2207	--	INCO 718	300	yes
Plasma spray	--	INCO 718	250	yes

*X40: Cobalt based X40 Superalloy.

**M246: Nickel based MAR-M246 superalloy.

Table 4: Chemical Analysis of Fly Ash

Chemical	Percentage
Silicon Dioxide (SiO_2)	48.08
Iron Oxide (Fe_2O_3)	20.05
Aluminide Oxide (Al_2O_3	21.16
Magnesium Oxide (MgO)	0.93
Sulphur Trioxide (SO_3)	1.20
Moisture Content	0.13
Loss of Ignition	0.73
Available Alkalies as Na_2O	0.64
Undetermined	7.08

Table 5. Typical Chromite Powder Analysis

Constituent	Typical Range
Chromium Oxide (Cr_2O_3)	45.5 - 46.5
Iron Oxide (FeO)	19.5 - 20.5
Alumina (Al_2O_3)	13.5 - 15.5
Magnesia (MgO)	9.3 - 10.5
Calcium Oxide (CaO)	0.2 - 0.4
Free Silica	0.8 - 1.5

Table 6. Material coefficients of Erosion Models

MATERIAL	a	C1	C2x10^2	n1	n2	n3	n4
FSX-414	1.05	0.18258	1.93233	2.90	0.50	2.40	3.13
IN-738	.85	0.02173	2.61691	2.57	0.40	2.40	2.77
M-246	5.40	0.418612	2.73895	2.32	0.60	2.25	2.94
X-40	0.95	0.1888266	2.25033	3.18	1.15	2.25	2.63
N	--	0.0510006	0.11602	3.31	1.35	3.0	3.22
RT22	--	0.0562133	0.052228	2.72	0.65	4.75	2.75
RT22B	--	0.027657	0.01216	3.70	1.5	4.3	3.73

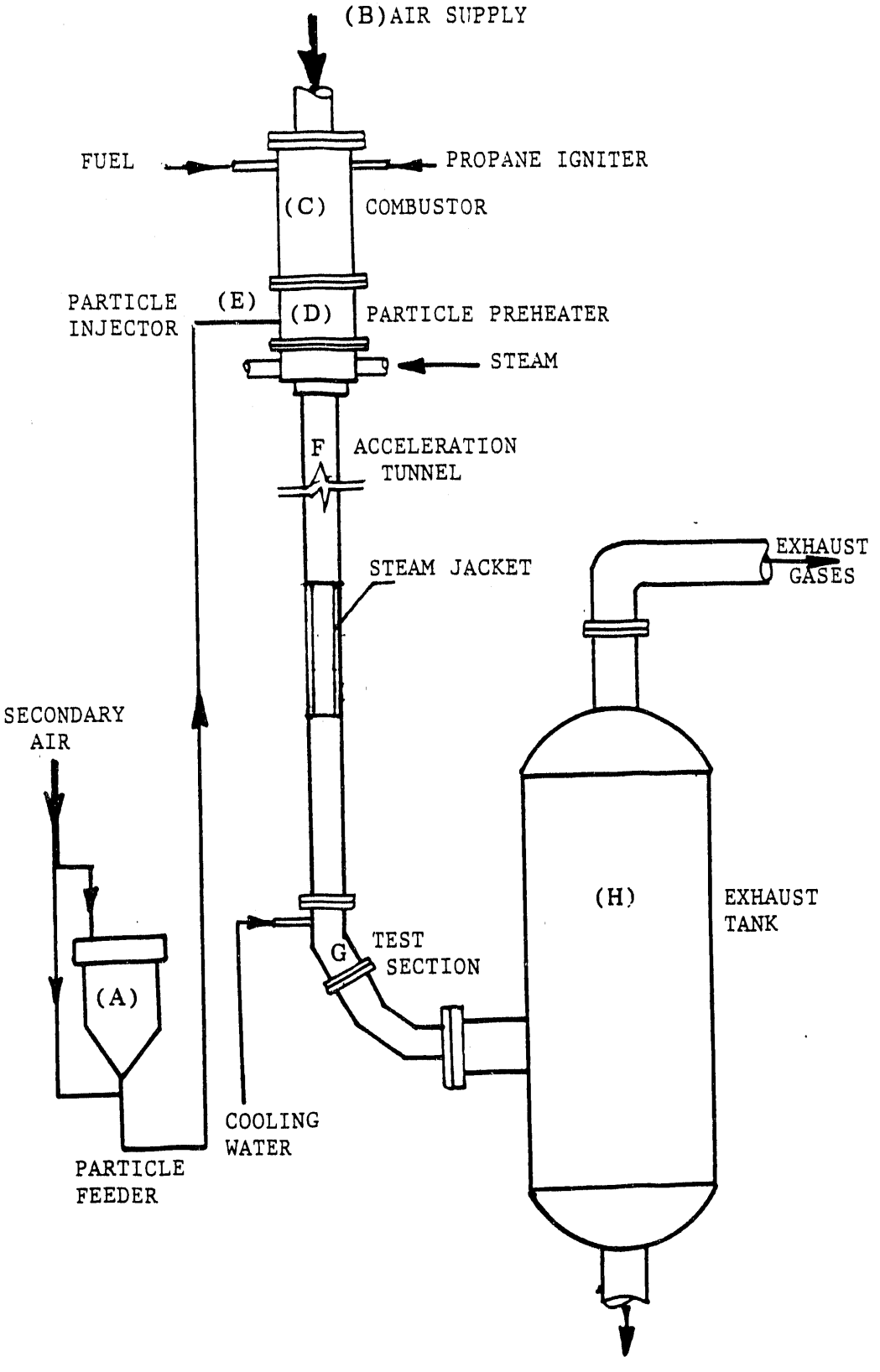

FIG. 1 SCHEMATIC OF EROSION TEST FACILITY

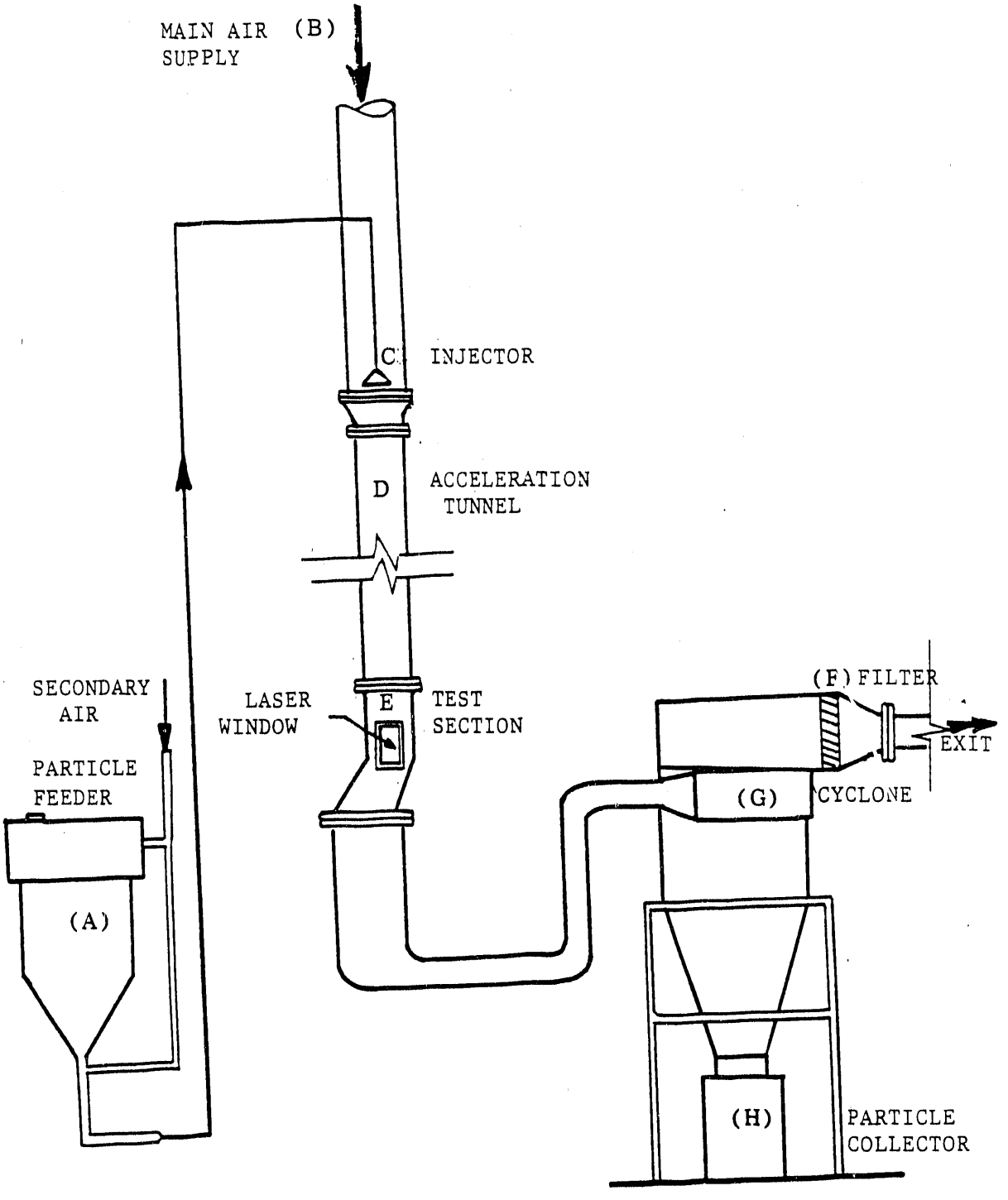

FIG. 2 SCHEMATIC OF REBOUND TEST FACILITY

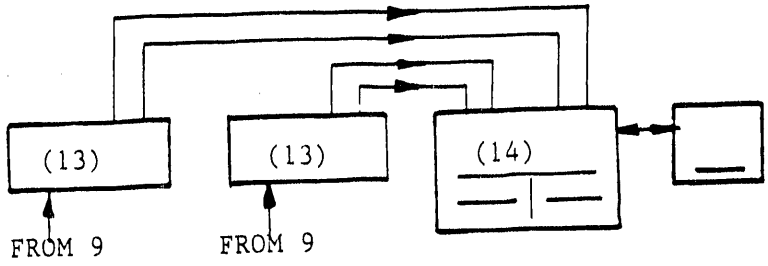

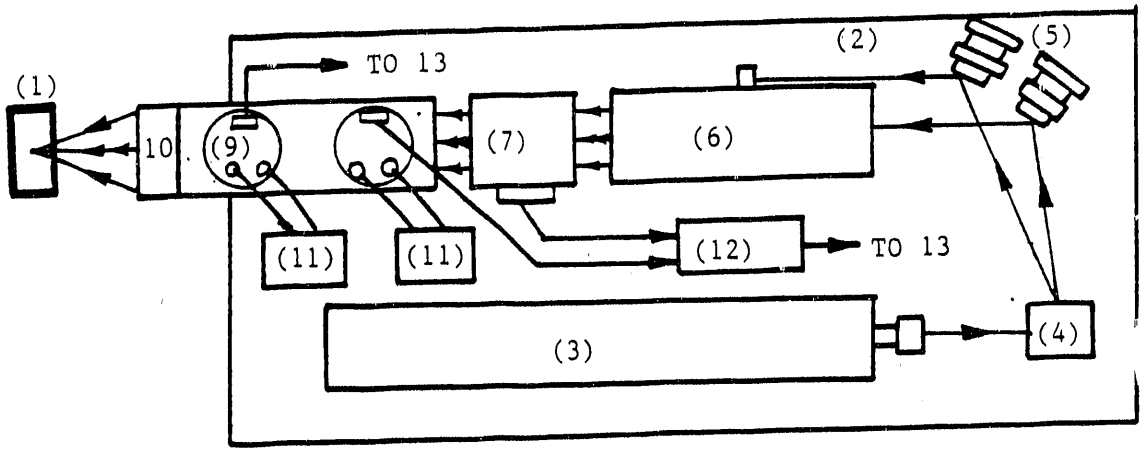

(1) TEST SECTION
(2) OPTICAL SYSTEM TABLE
(3) LASER TUBE
(4) DISPERSION PRISM
(5) MIRRORS
(6) BEAMSPLITTER
(7) FREQUENCY SHIFTER
(8) RECEIVING OPTICS
(9) PHOTODETECTOR
(10) COLLECTING LENS
(11) PHOTOMULTIPLIER
(12) FREQUENCY DOWNMIXER
(13) DATA PROCESSORS
(14) PC COMPUTER

FIG. 3 SCHEMATIC OF LDV EXPERIMENTAL SET-UP

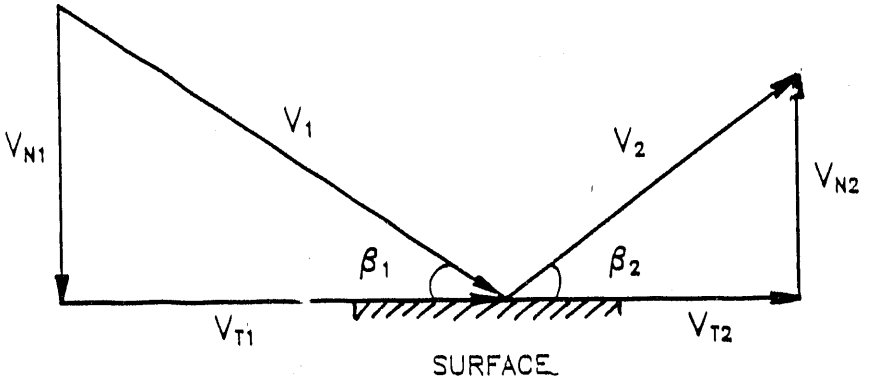

FIG. 4 REBOUND VELOCITY AND ANGLE NOTATIO

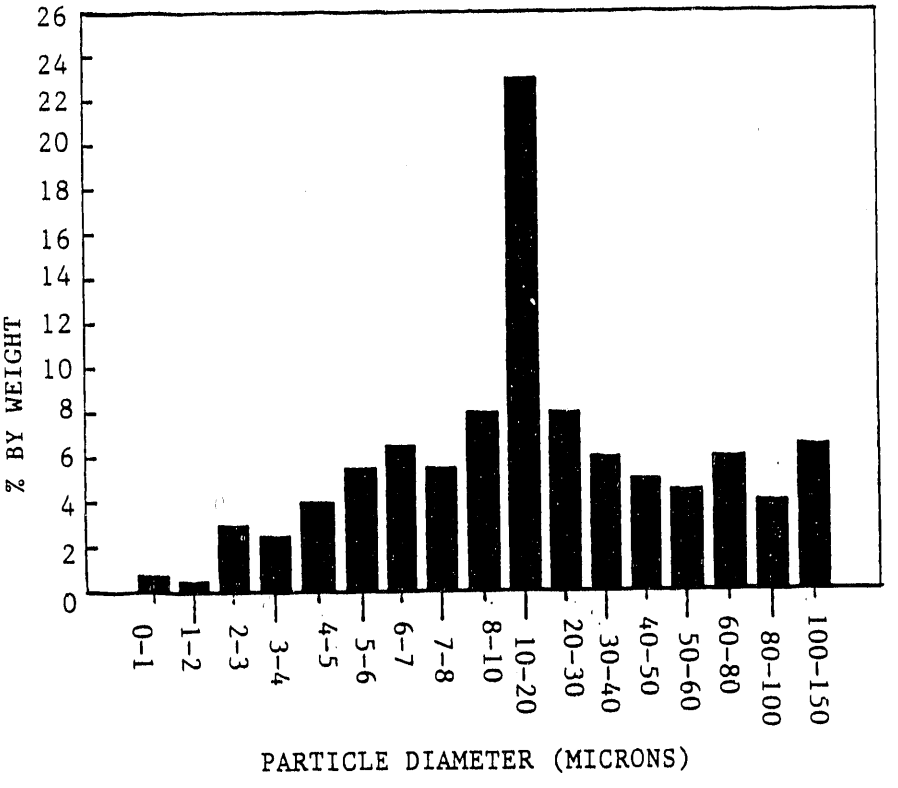

FIG. 5 FLY ASH PARTICLE SIZE DISTRIBUTION.

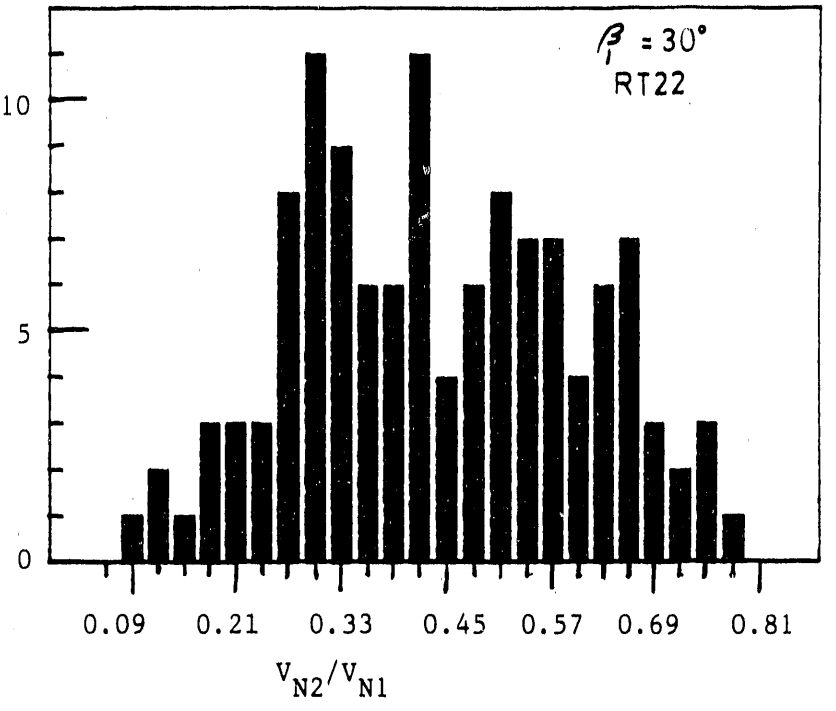

Fig. 6 . Normal Velocity Restitution Ratio Distribution.

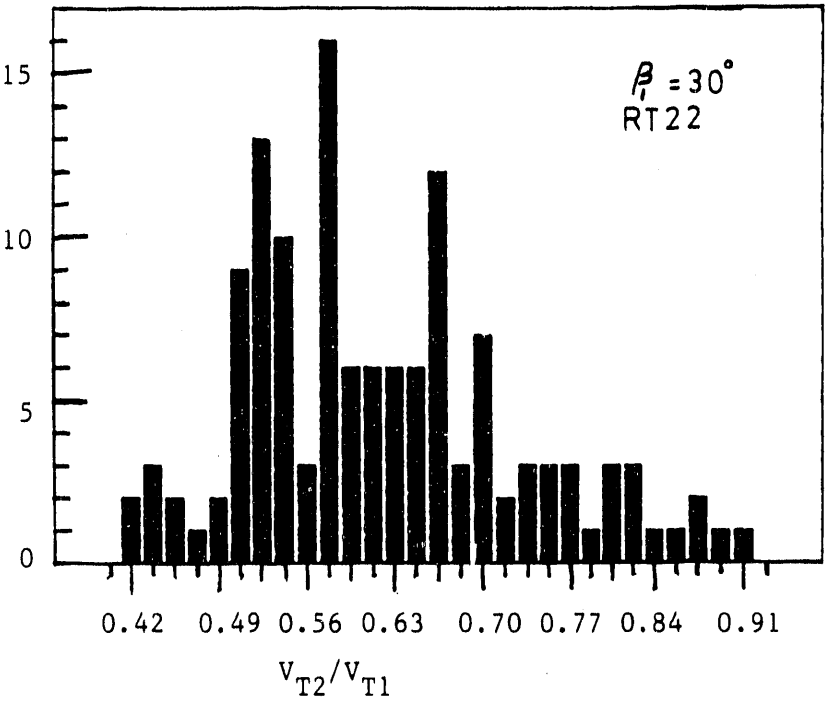

Fig. 7 . Tangential Velocity Restitution Ratio Distribution.

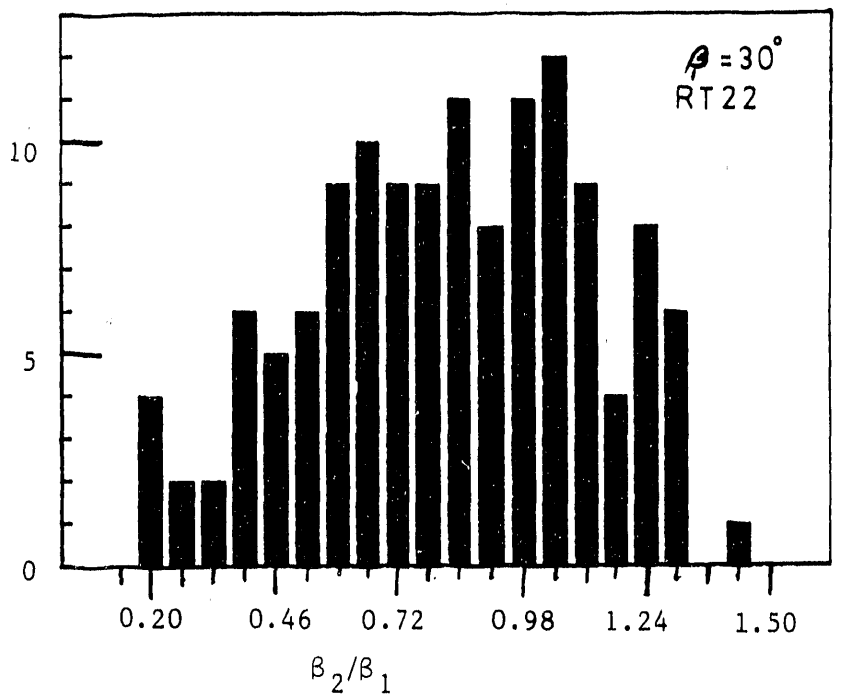

Fig. 8 . Directional Restitution Ratio Distribution.

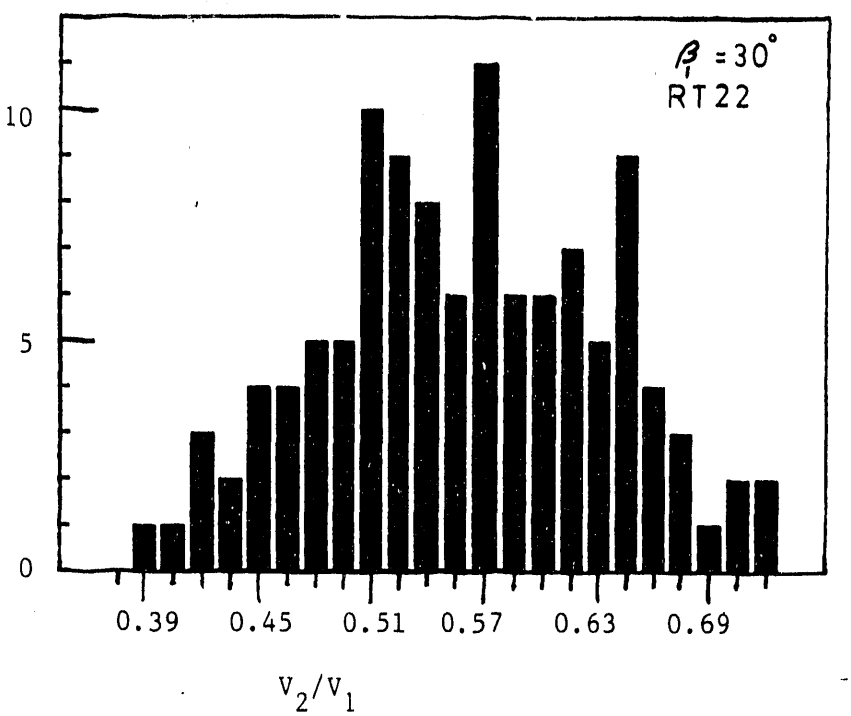

Fig. 9. Total Velocity Restitution Ratio Distribution.

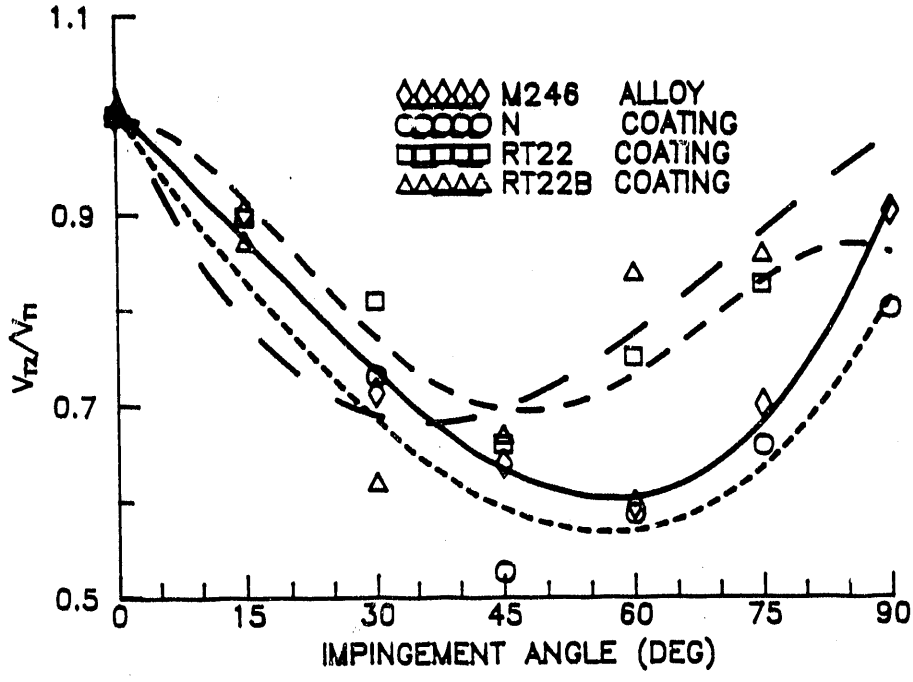

FIG. 10 TANGENTIAL VELOCITY RESTITUTION RATIO OF M246 ALLOY AND N, RT22 & RT22B COATINGS: V_1=320 fps, FLY ASH PARTICLES

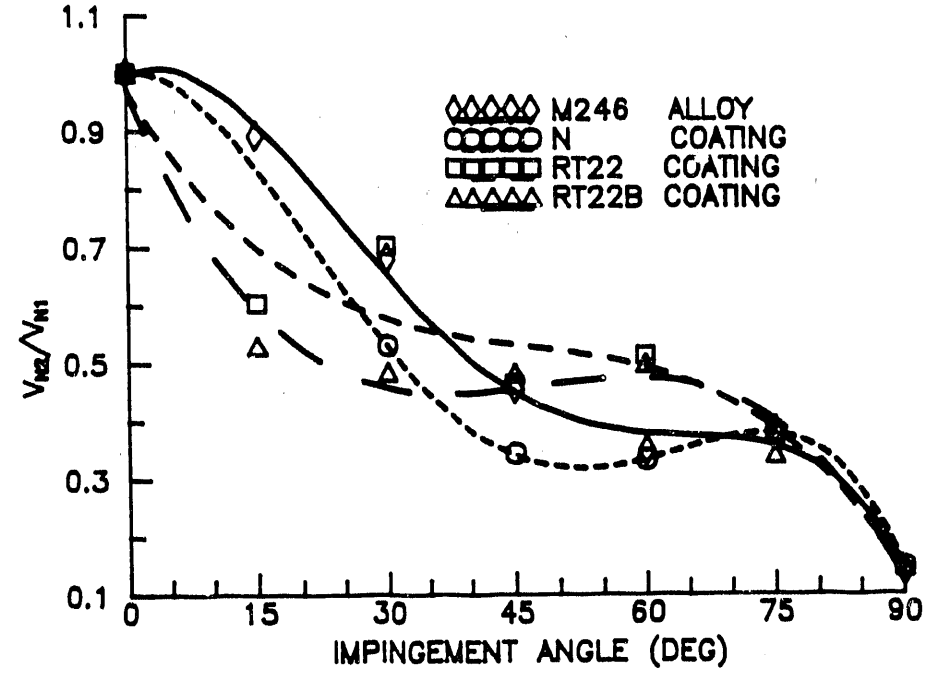

FIG. 11 NORMAL VELOCITY RESTITUTION RATIO OF M246 ALLOY AND N, RT22 & RT22B COATINGS: V_1=320 fps, FLY ASH PARTICLES.

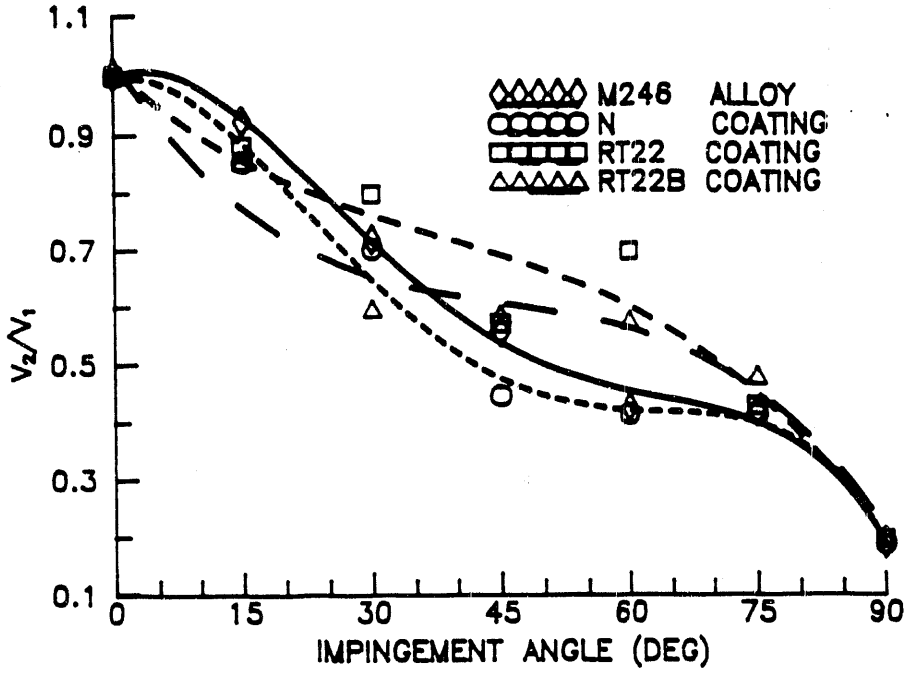

FIG. 12 TOTAL VELOCITY RESTITUTION RATIO OF M246 ALLOY AND N, RT22 & RT22B COATINGS: V_1=320 fps, FLY ASH PARTICLES.

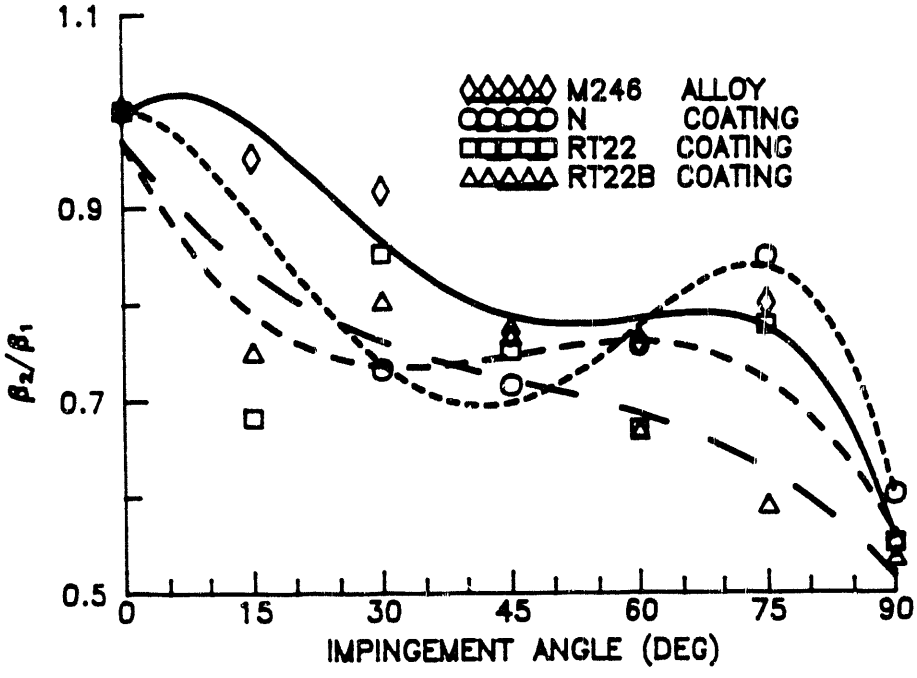

FIG. 13 DIRECTIONAL RESTITUTION RATIO OF M246 ALLOY AND N, RT22 & RT22B COATINGS: V_1=320 fps, FLY ASH PARTICLES

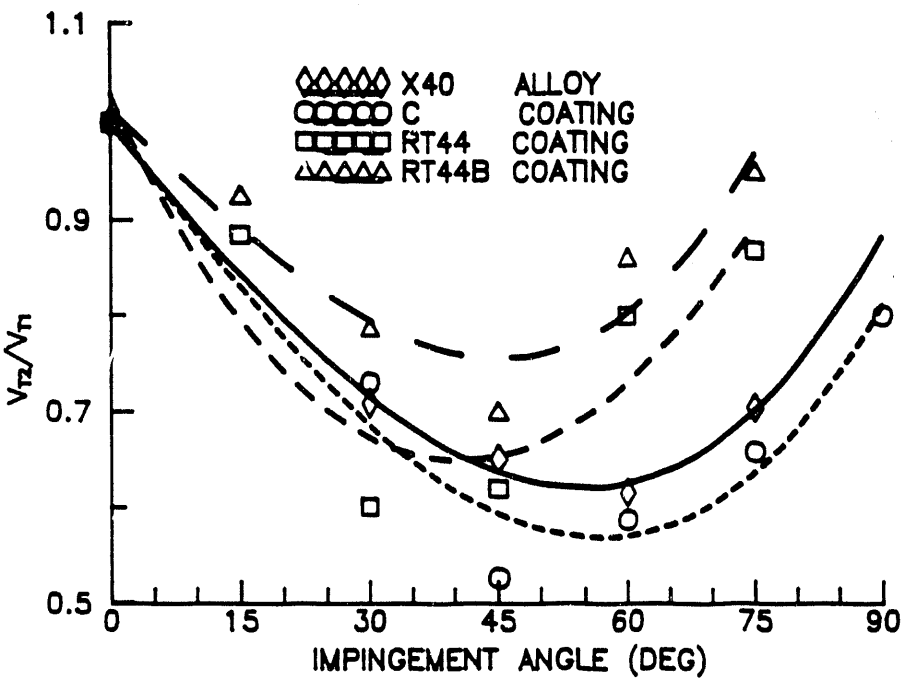

FIG. 14 TANGENIAL VELOCITY RESTITUTION RATIO OF X40 ALLOY AND C, RT44 & RT44B COATINGS: V_1=320 fps, FLY ASH PARTICLES.

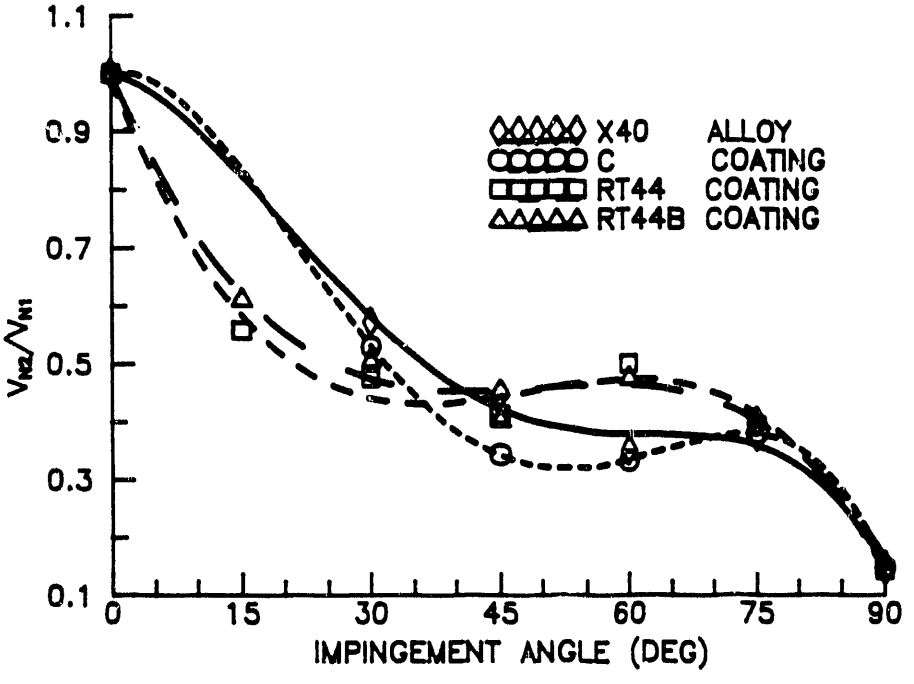

FIG. 15 NORMAL VELOCITY RESTITUTION RATIO OF X40 ALLOY AND C, RT44 & RT44B COATINGS: V_1=320 fps, FLY ASH PARTICLES.

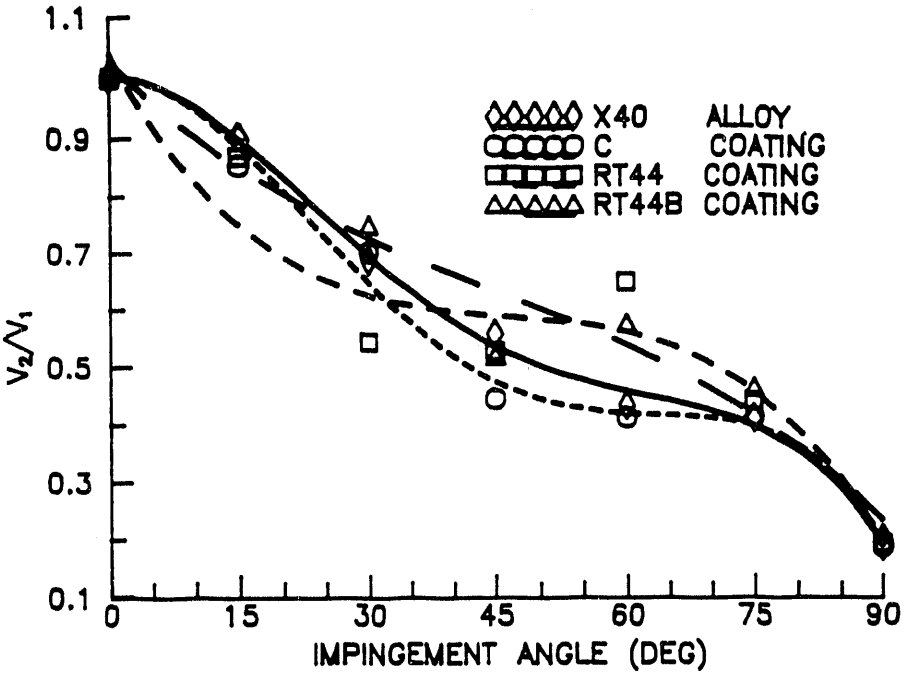

FIG. 16 TOTAL VELOCITY RESTITUTION RATIO OF X40 ALLOY AND C, RT44 & RT44B COATINGS: V_1=320 fps, FLY ASH PARTICLES.

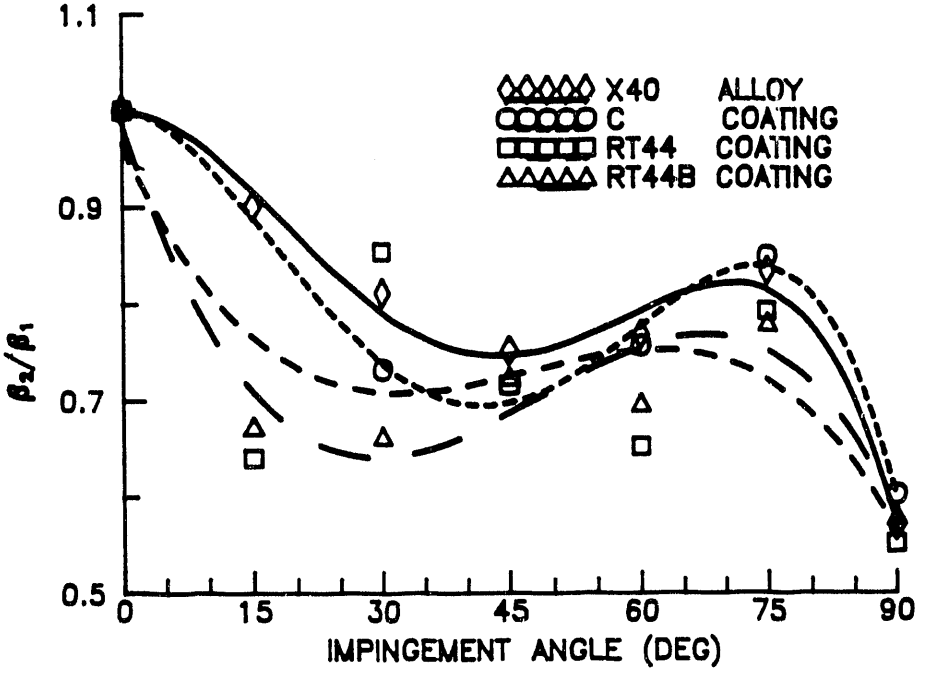

FIG. 17 DIRECTIONAL RESTITUTION RATIO OF X40 ALLOY AND C, RT44 & RT44B COATINGS: V_1=320 fps, FLY ASH PARTICLES.

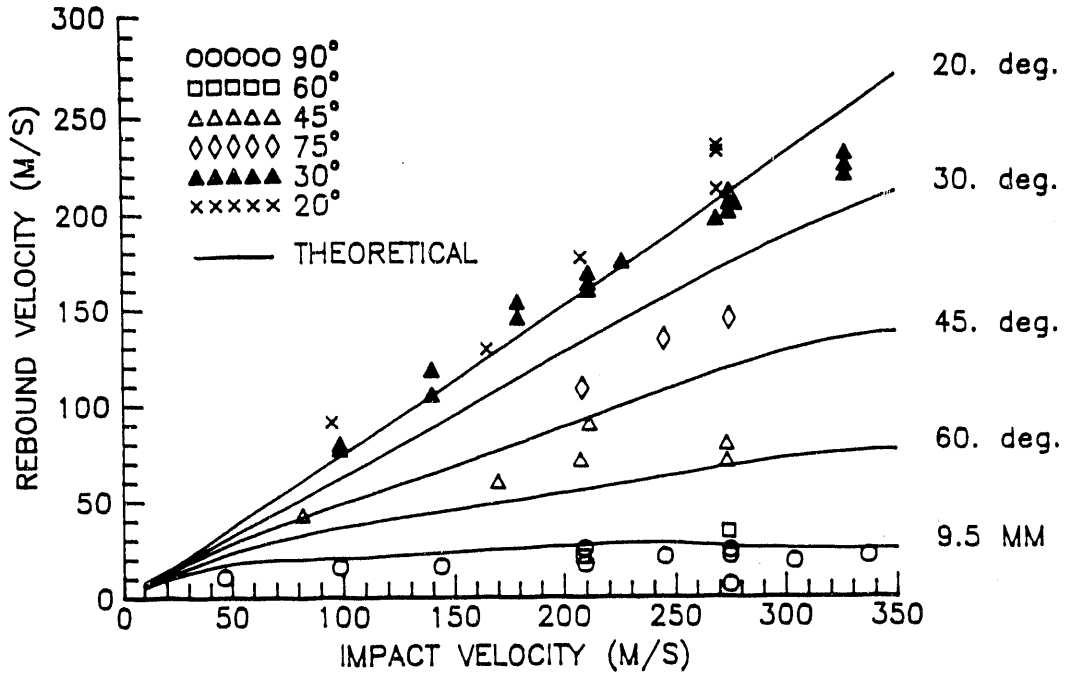

FIG. 18 PARTICLE REBOUND VELOCITY VARIATION WITH IMPACT VELOCITY FOR DIFFERENT IMPACT ANGLES

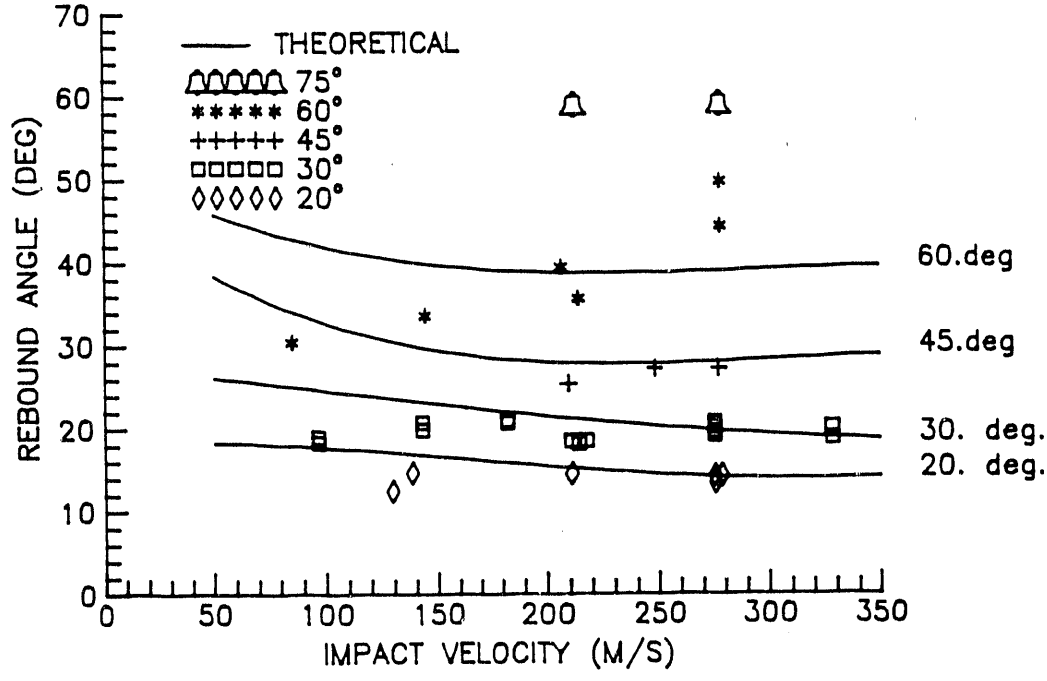

FIG. 19 PARTICLE REBOUND ANGLE VARIATION WITH IMPACT VELOCITY FOR DIFFERENT IMPACT ANGLES

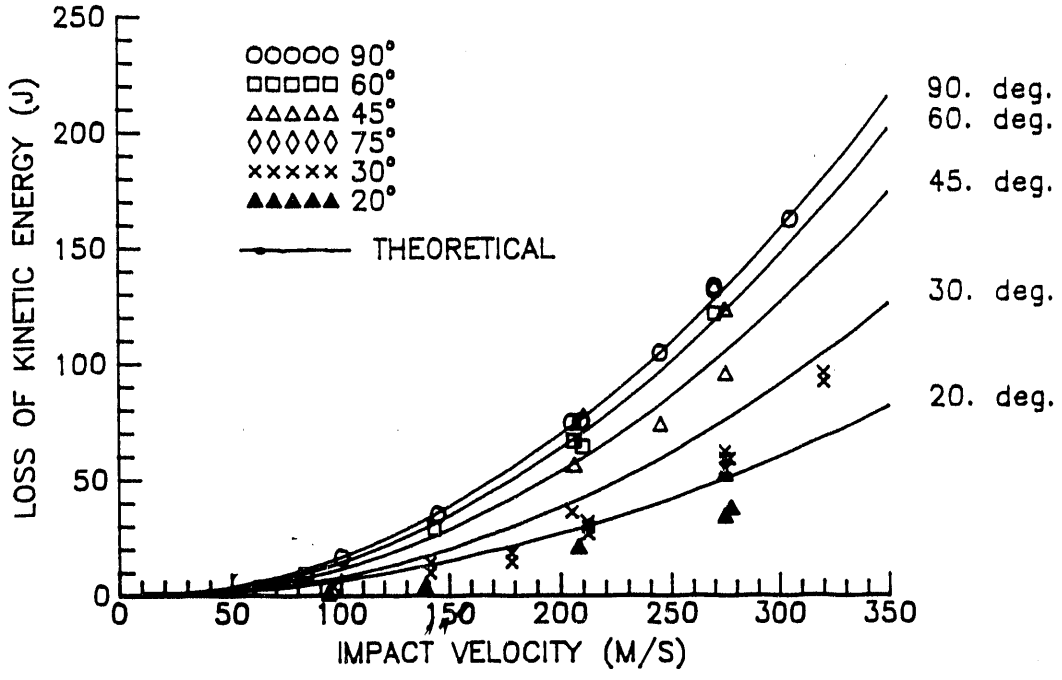

FIG. 20 PARTICLE KINETIC ENERGY LOSS VARIATION WITH IMPACT VELOCITY FOR DIFFERENT IMPACT ANGLES

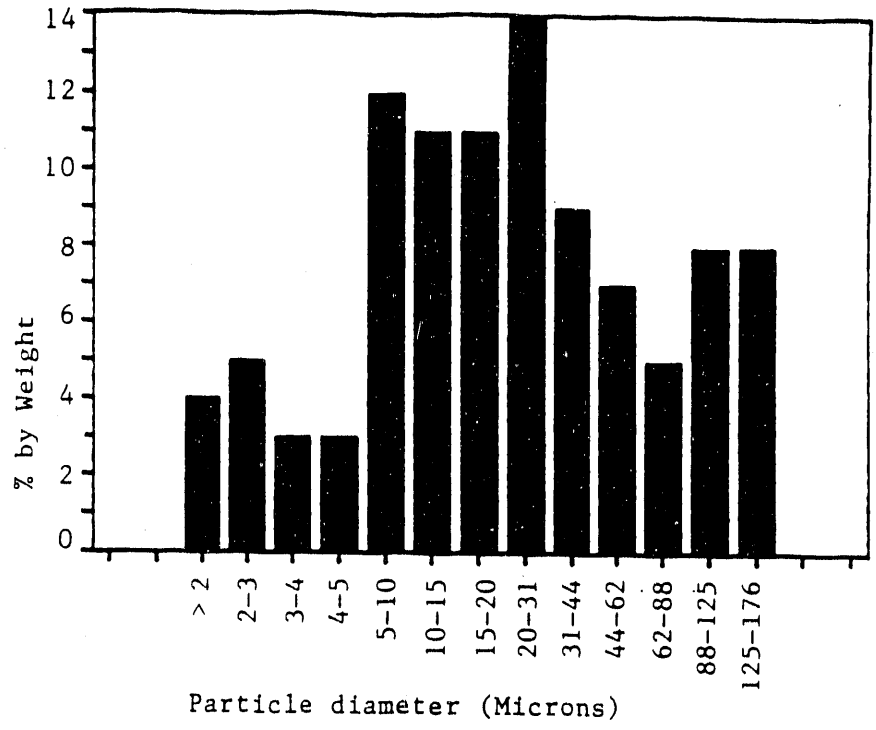

FIG. 21 CHROMITE PARTICLE SIZE DISTRIBUTION

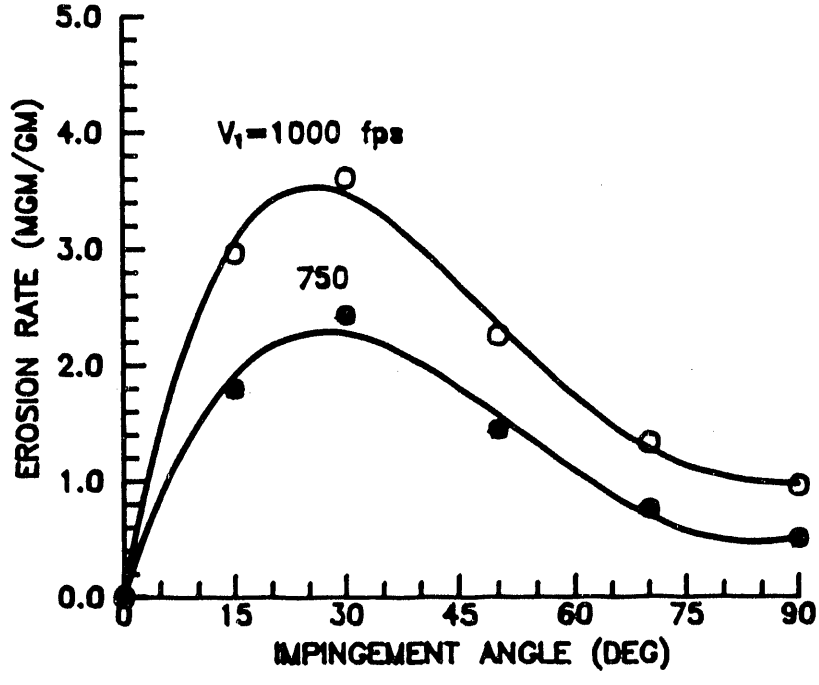

FIG. 22 410 STAINLESS STEEL EROSION RATE VARIATION WITH IMPINGEMENT ANGLE: T=1022 F, CHROMITE PARTICLES

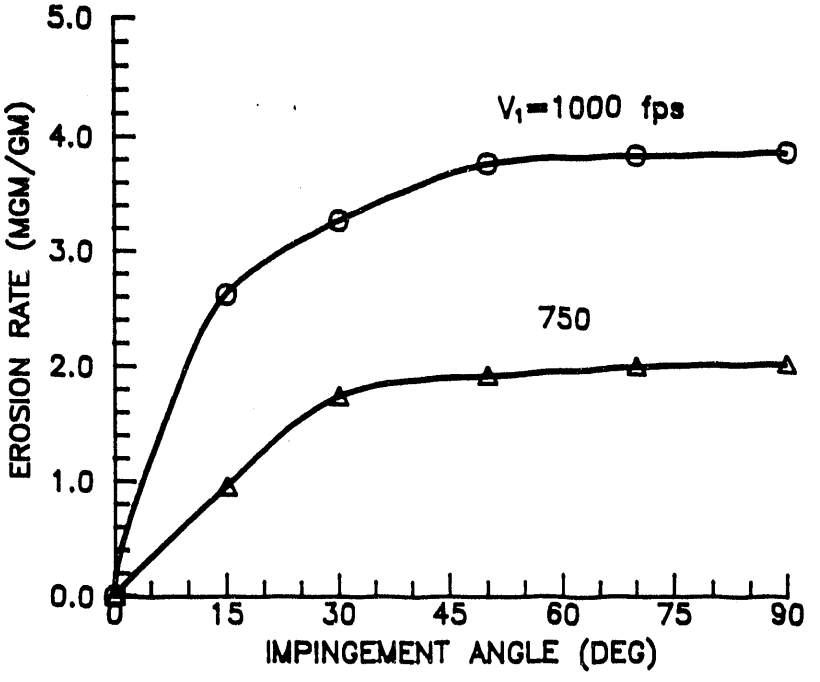

FIG. 23 LC-1B COATING EROSION RATE VARIATION WITH IMPINGEMENT ANGLE: T=1022 F, CHROMITE PARTICLES

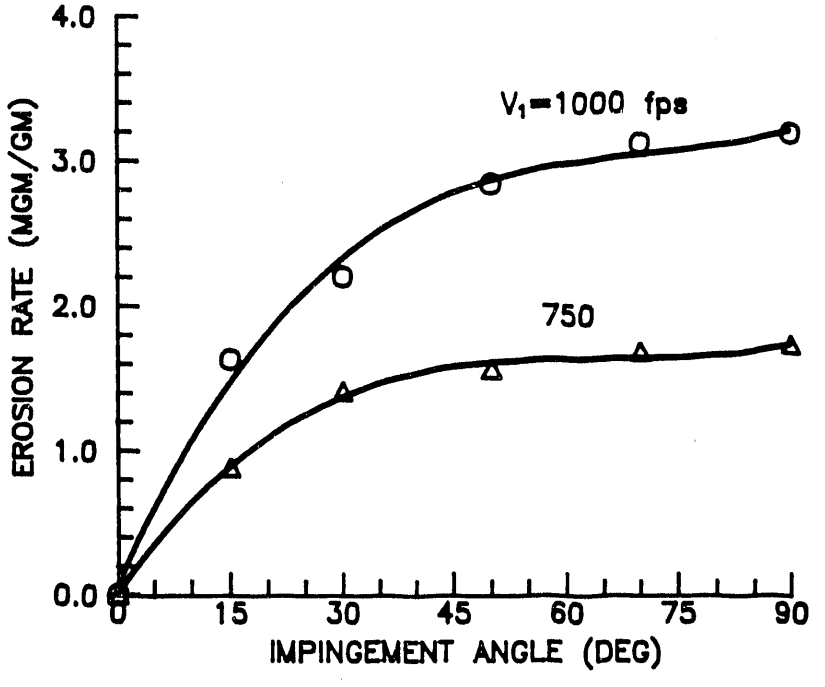

FIG. 24 LC-1H COATING EROSION RATE VARIATION WITH IMPINGEMENT ANGLE: T=1022 F, CHROMITE PARTICLES

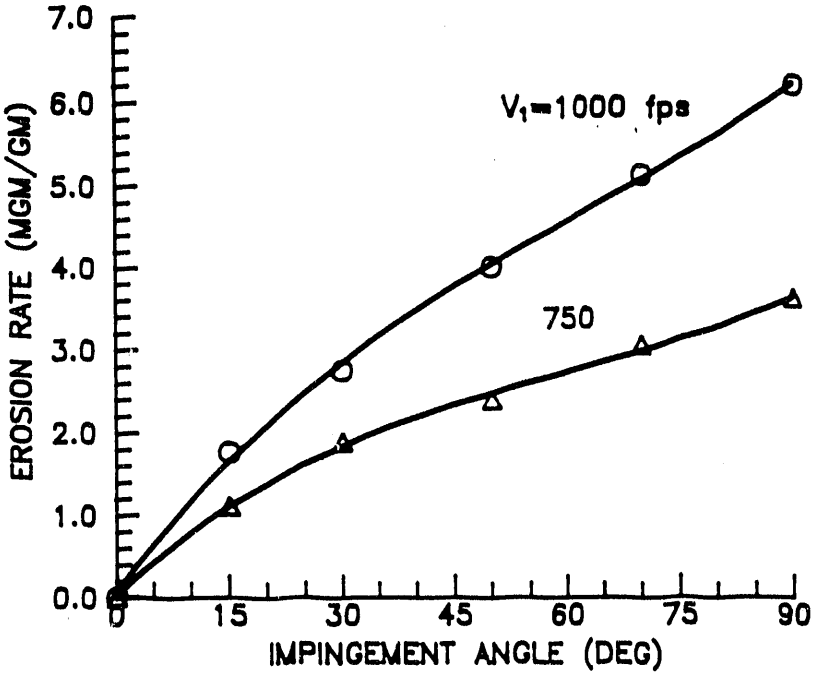

FIG. 25 PLASMA SPRAY COATING EROSION RATE VARIATION WITH IMPINGEMENT ANGLE: T=1022 F, CHROMITE PARTICLES

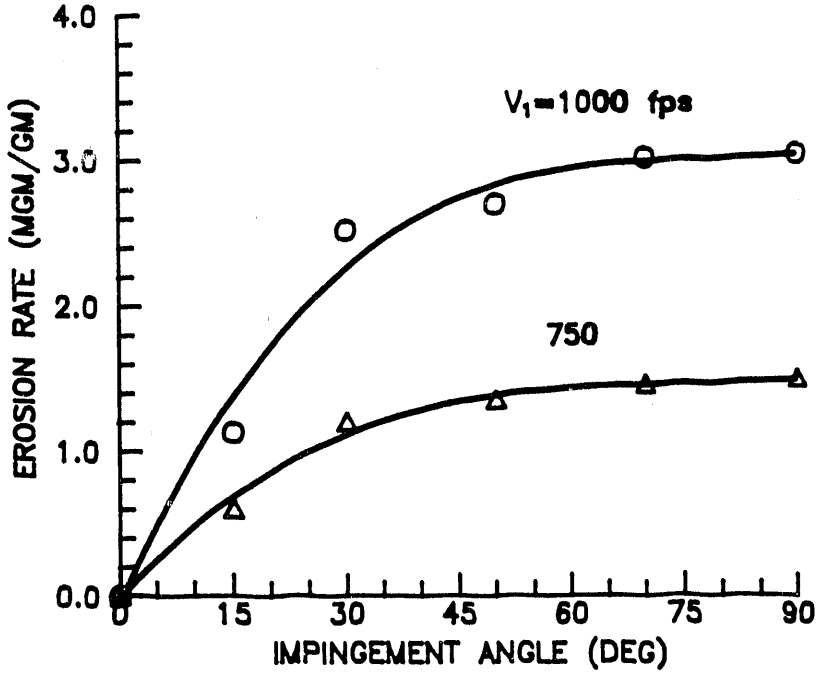

FIG. 26 SDG-2207 COATING EROSION RATE VARIATION WITH IMPINGEMENT ANGLE: T=1022 F, CHROMITE PARTICLES

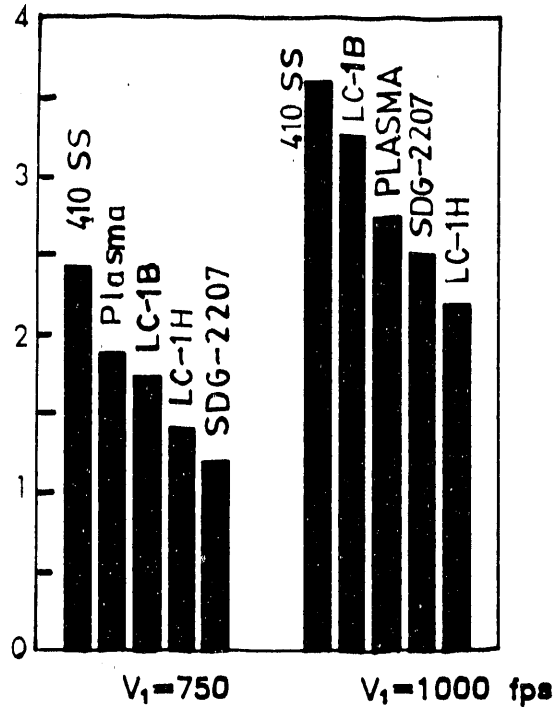

FIG. 27 COMPARISON OF EROSION RATES OF COATINGS AND 410 STAINLESS STEEL ALLOY: $\beta_1=30°$,CHROMITE PARTICLES

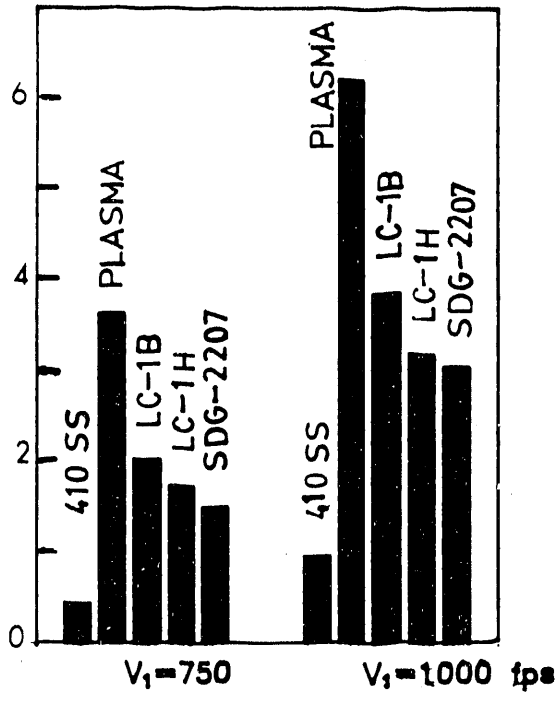

FIG. 28 COMPARISON OF EROSION RATES OF COATINGS AND 410 STAINLESS STEEL ALLOY: $\beta_1=90°$,CHROMITE PARTICLES

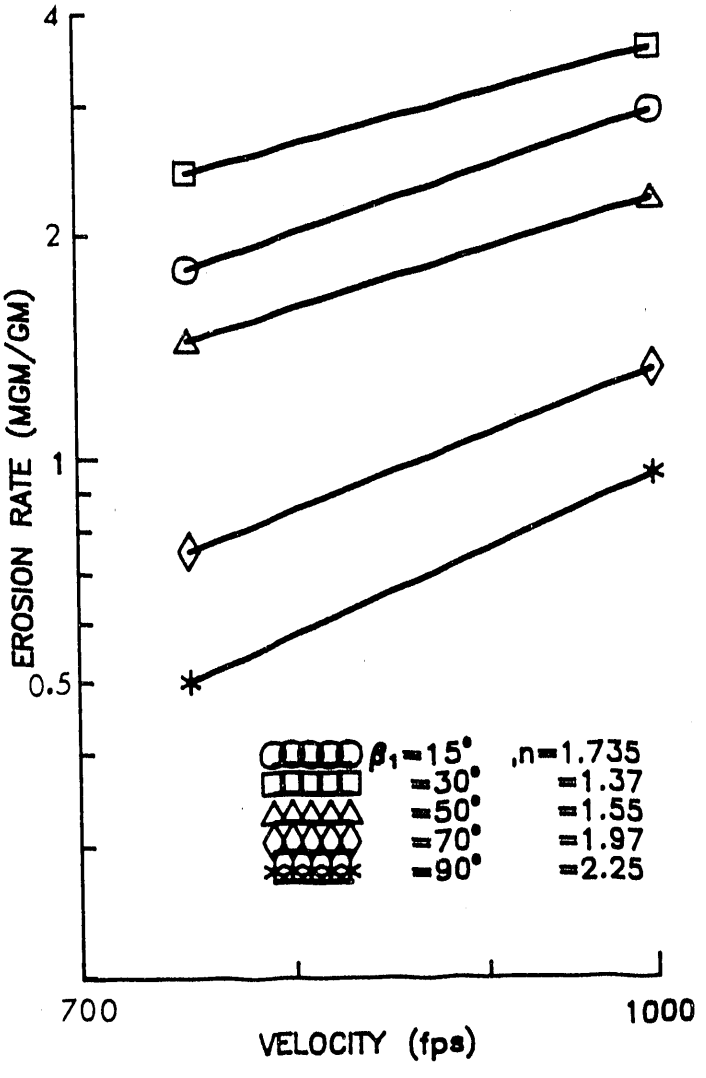

FIG. 29 VELOCITY EFFECT ON 410 STAINLESS STEEL EROSION RATE AT DIFFERENT ANGLES: T=1022 F, CHROMITE PARTICLES.

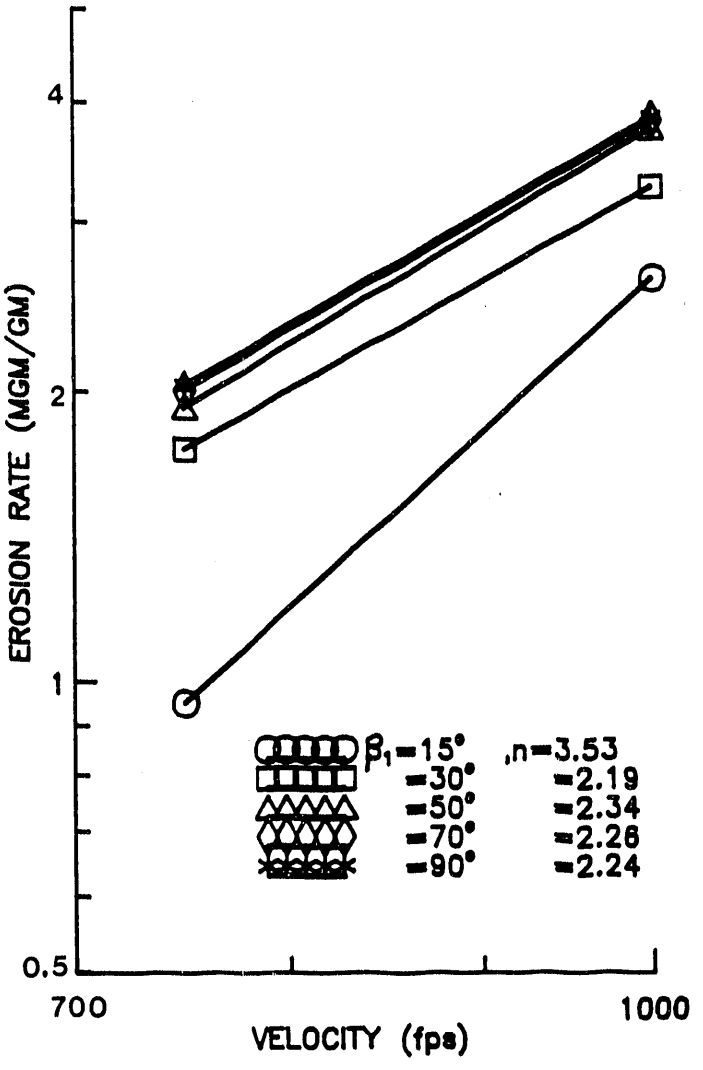

FIG. 30 VELOCITY EFFECT ON LC-1B COATING EROSION RATE AT DIFFERENT ANGLES: T=1022 F, CHROMITE PARTICLES

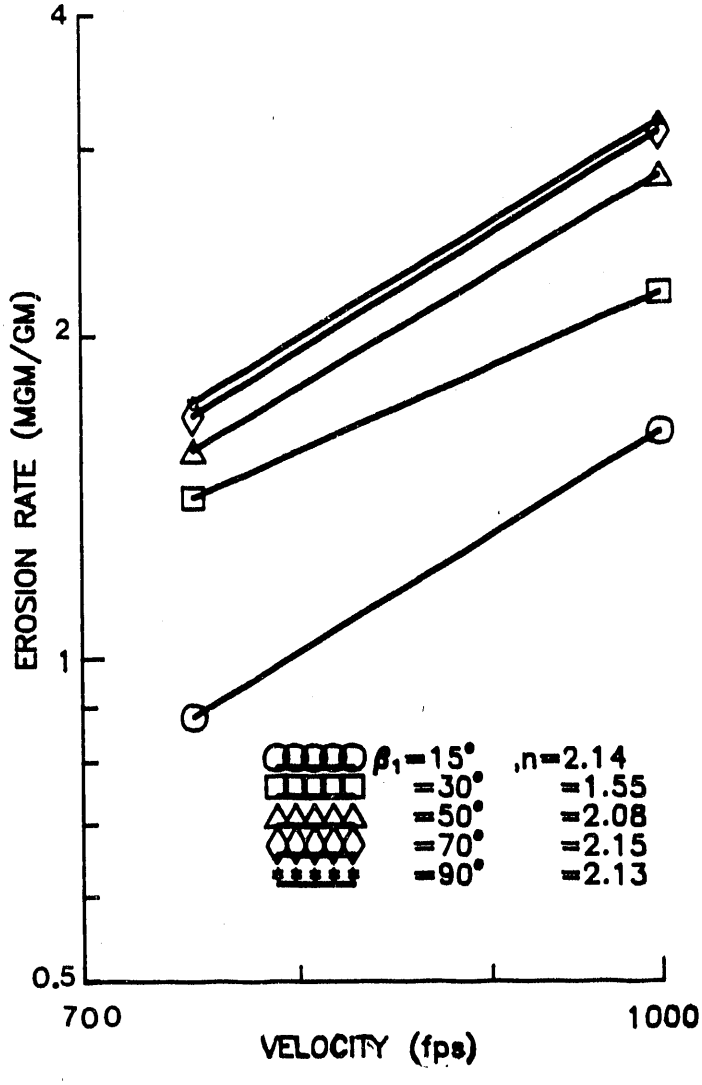

FIG. 31 VELOCITY EFFECT ON LC-1H COATING EROSION RATE AT DIFFERENT ANGLES: T=1022 F, CHROMITE PARTICLES

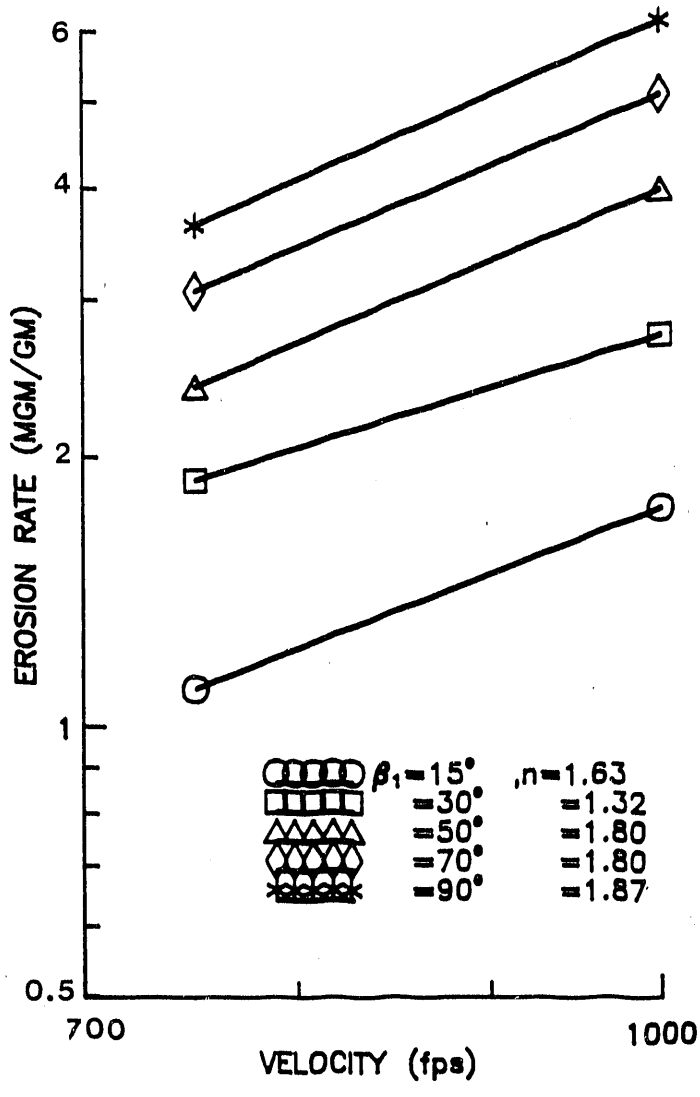

FIG. 32 VELOCITY EFFECT ON PLASMA SPRAY COATING EROSION RATE AT DIFFERENT ANGLES: T=1022 F, CHROMITE PARTICLES.

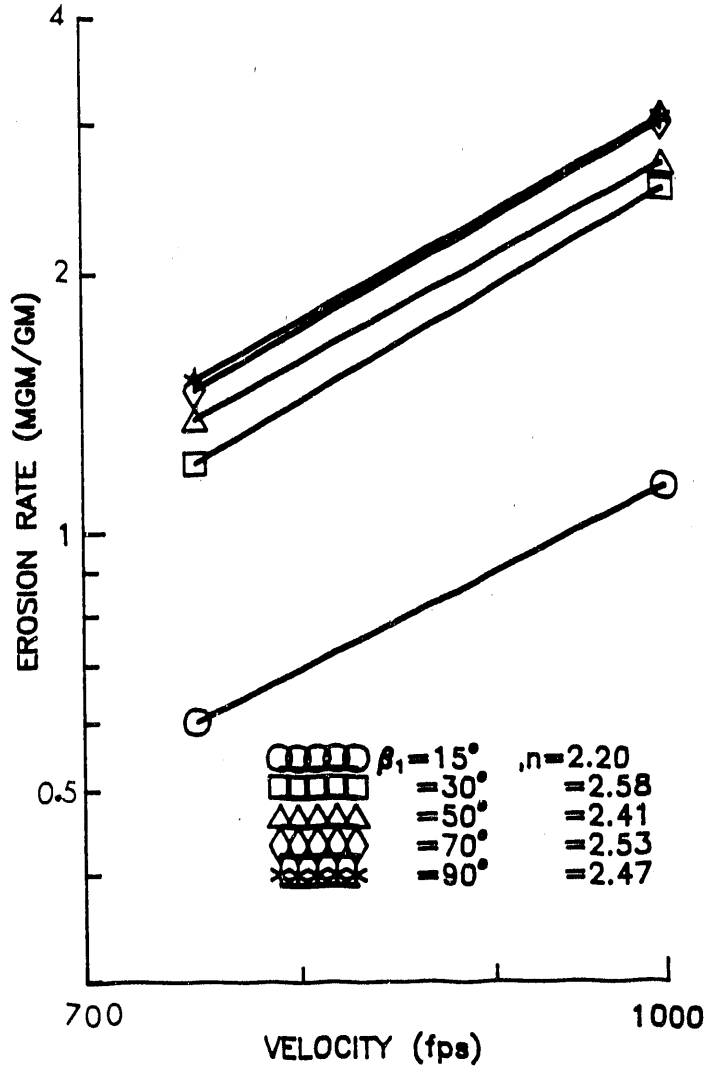

FIG. 33 VELOCITY EFFECT ON SDG-2207 COATING EROSION RATE AT DIFFERENT ANGLES: T=1022 F, CHROMITE PARTICLES.

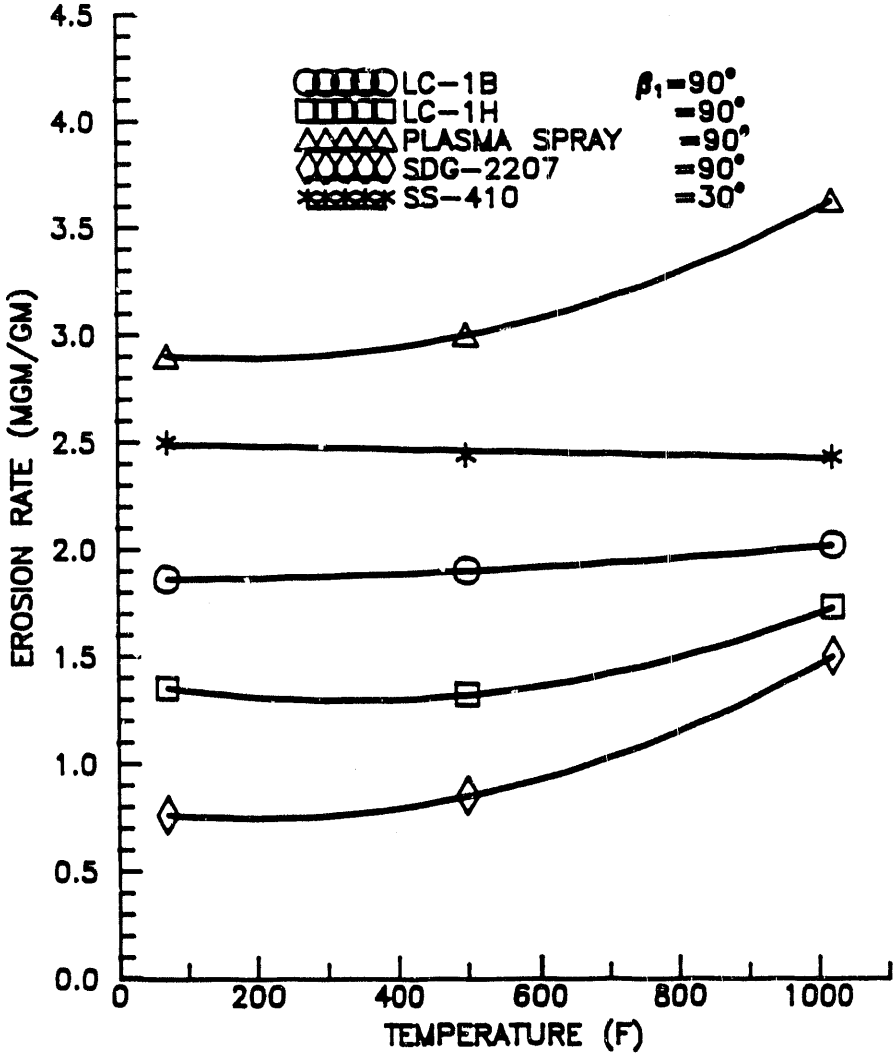

FIG. 34 VARIATION OF EROSION RATE WITH TEMPERATURE FOR LC-1B, LC-1H, SDG-2207 AND PLASMA SPRAY COATINGS AND 410 STAINLESS STEEL: V_1=750 fps , CHROMITE PARTICLES

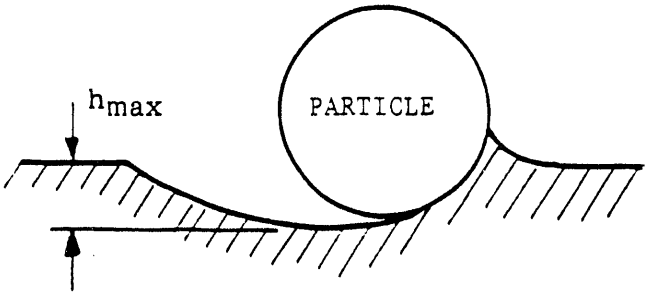

(a) Actual

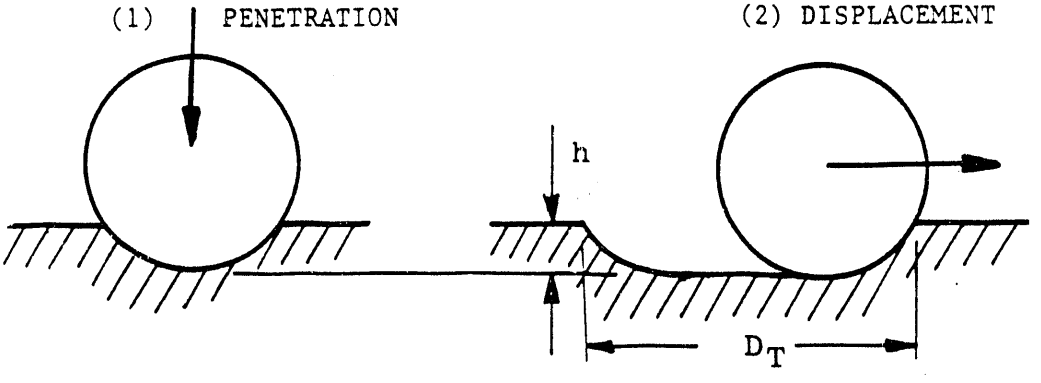

(b) Theoritical

FIG. 35 SCHEMATIC OF THEORITICAL AND ACTUAL EROSION PROCESS.

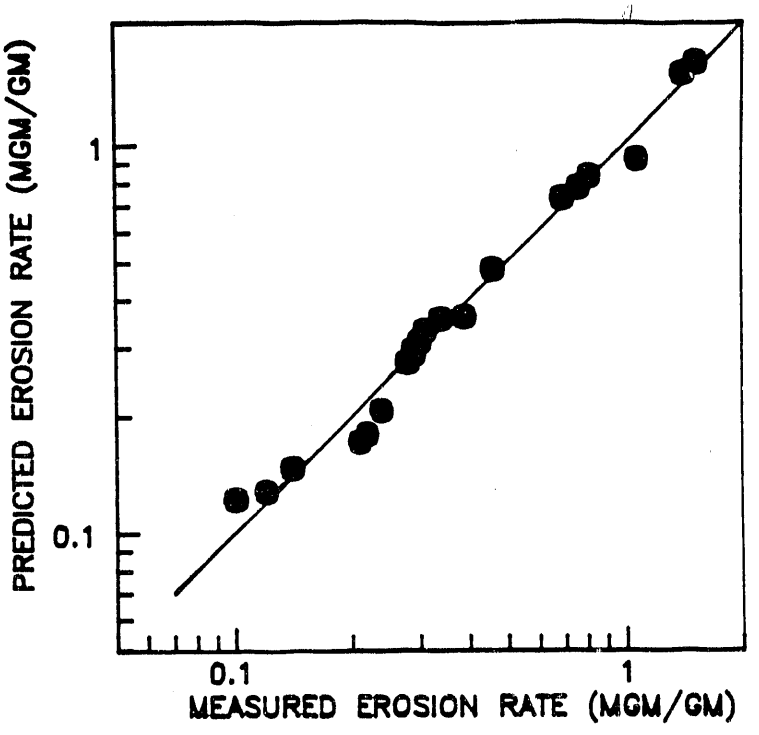

FIG. 36 COMPARISON BETWEEN MEASURED AND PREDICTED EROSION RATES FOR FSX-414 ALLOY

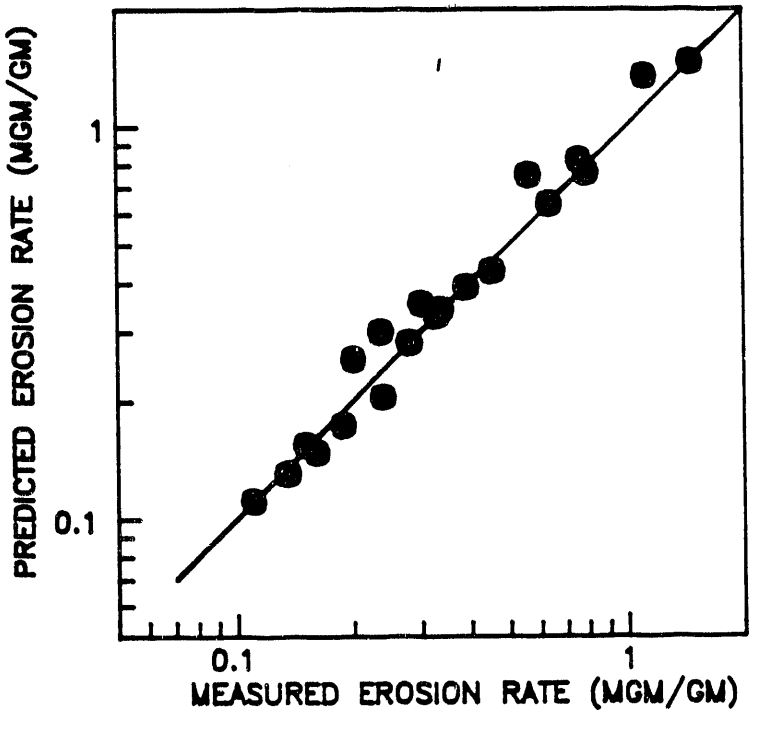

FIG. 37 COMPARISON BETWEEN MEASURED AND PREDICTED EROSION RATES FOR IN-738 ALLOY

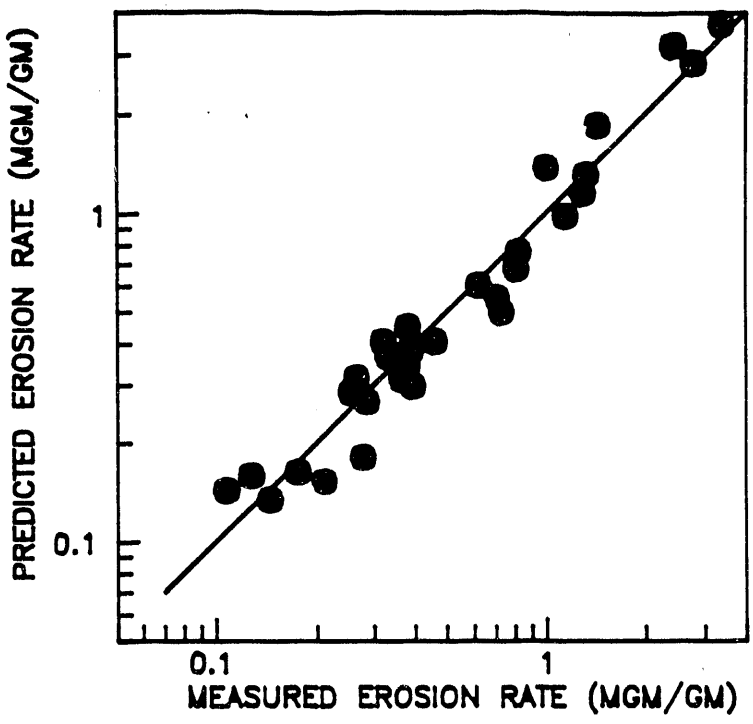

FIG. 38 COMPARISON BETWEEN MEASURED AND PREDICTED EROSION RATES FOR M246 ALLOY

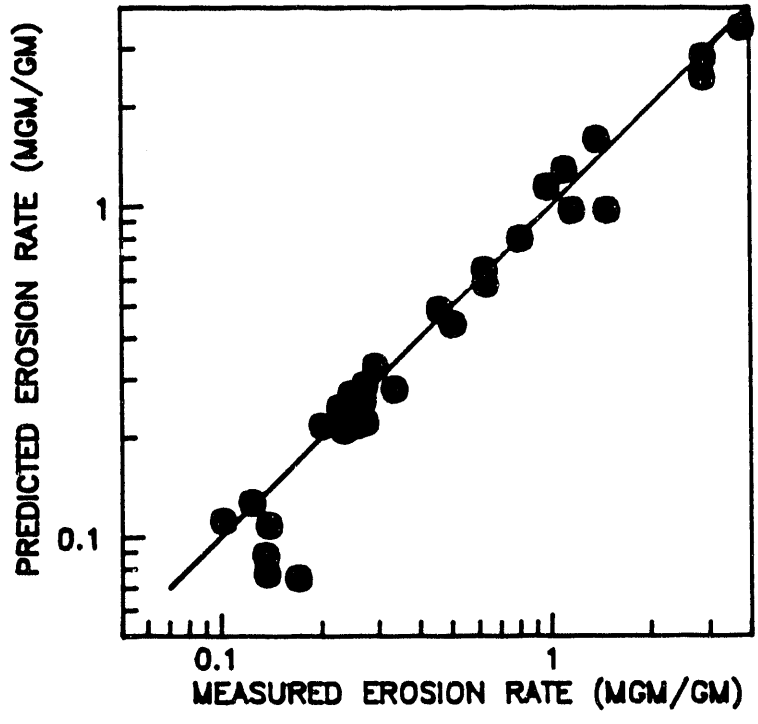

FIG. 39 COMPARISON BETWEEN MEASURED AND PREDICTED EROSION RATES FOR X40 ALLOY

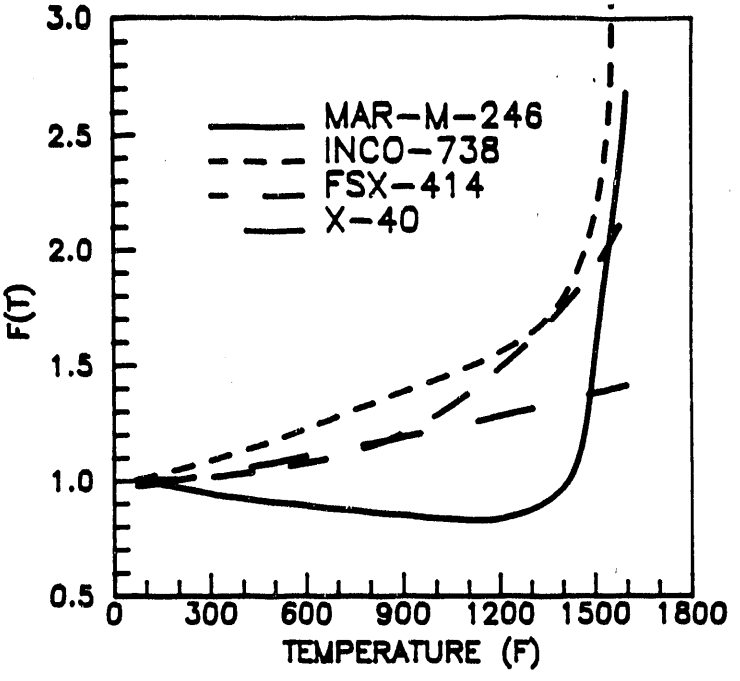

FIG. 40 VARIATION OF SUPERALLOY TEMPERATURE PARAMETERS WITH TEMPERATURE

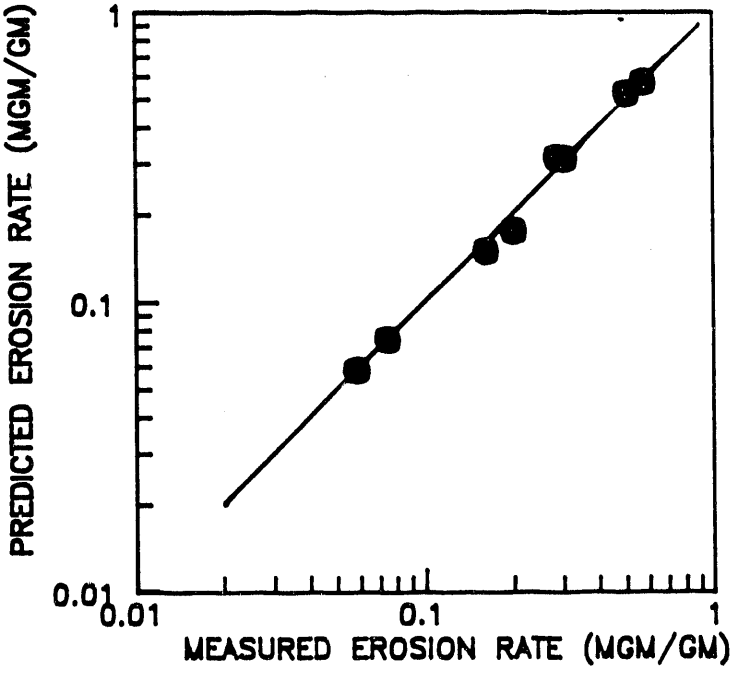

FIG. 41 COMPARISON BETWEEN MEASURED AND PREDICTED EROSION RATES FOR N COATING

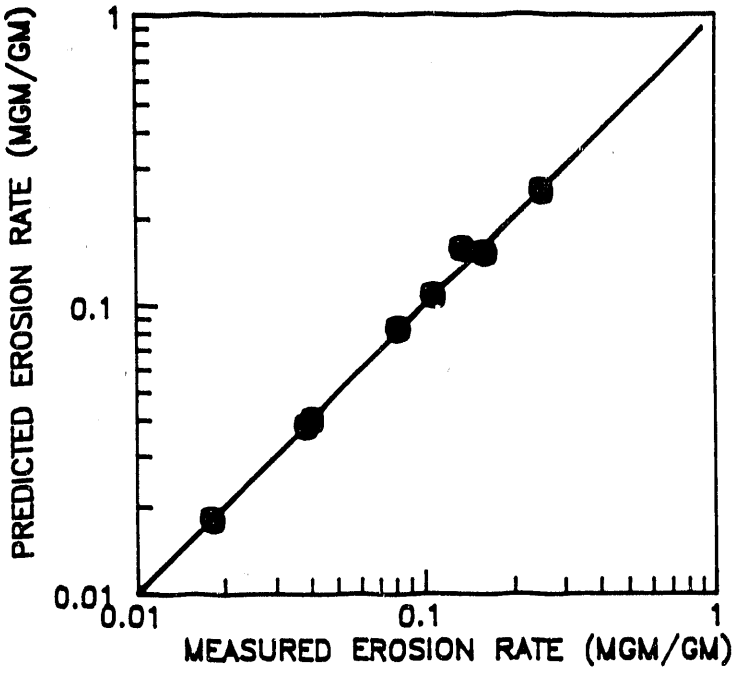

FIG. 42 COMPARISON BETWEEN MEASURED AND PREDICTED EROSION RATES FOR RT22 COATING

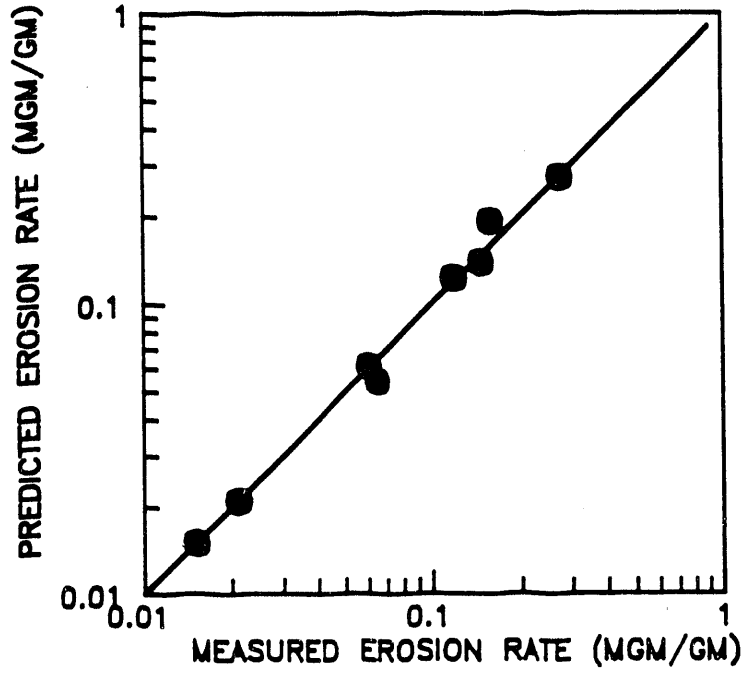

FIG. 43 COMPARISON BETWEEN MEASURED AND PREDICTED EROSION RATES FOR RT22B COATING

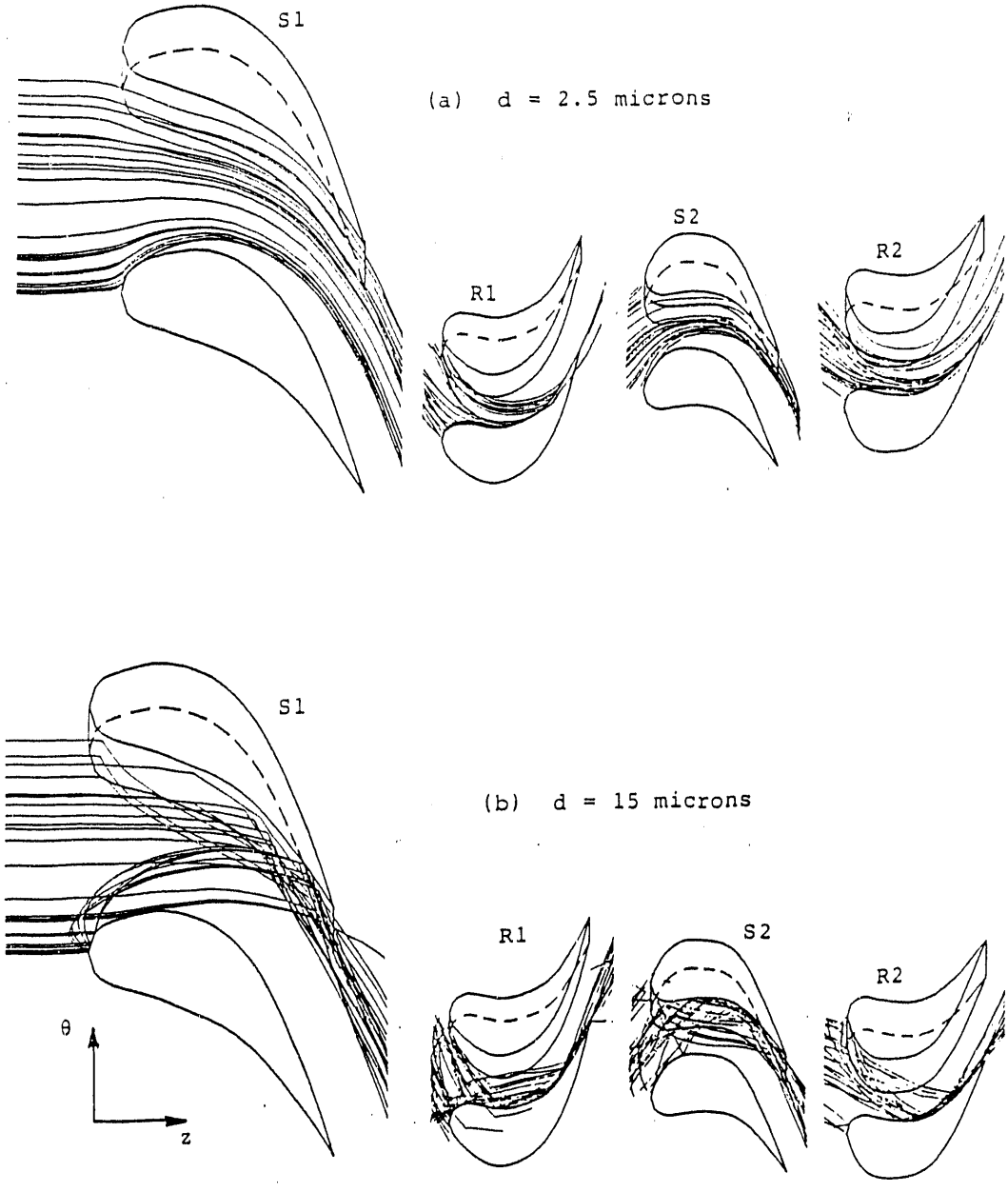

FIG. 44 PROJECTION OF PARTICLE TRAJECTORIES IN θ-z PLANE.

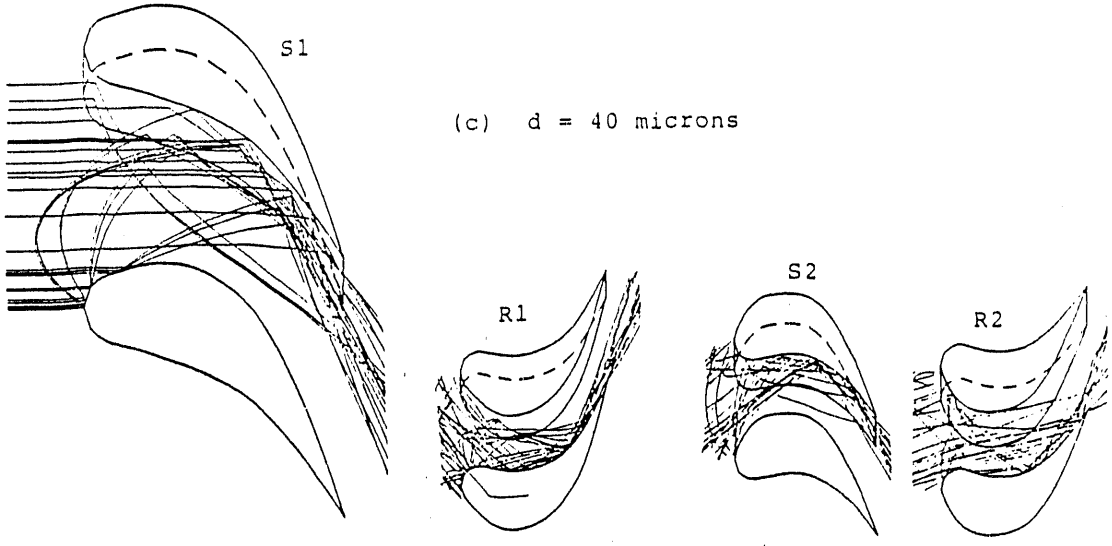

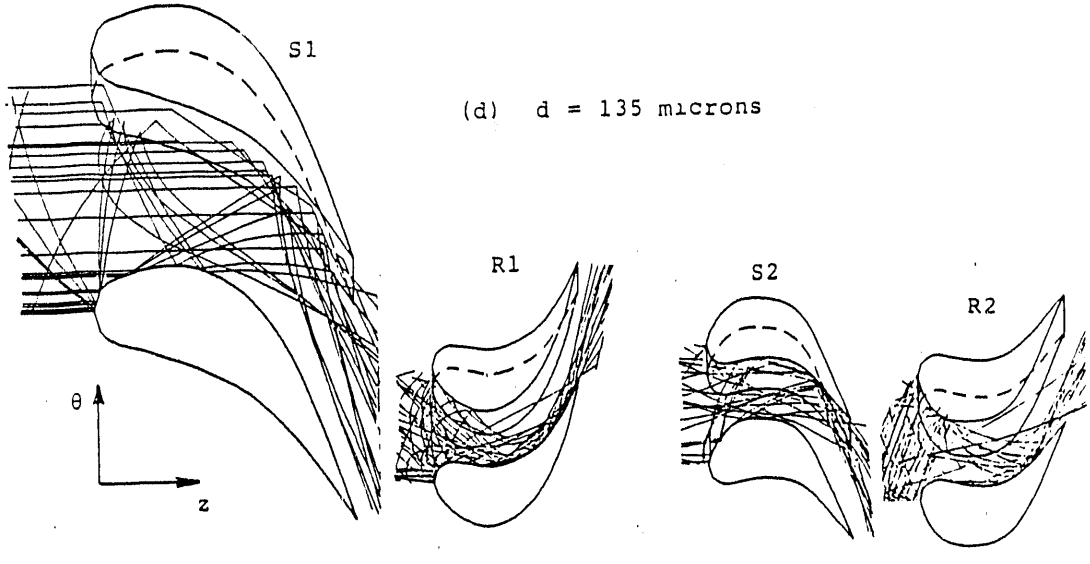

FIG. 44 PROJECTION OF PARTICLE TRAJECTORIES IN θ-z PLANE (CONT'D.).

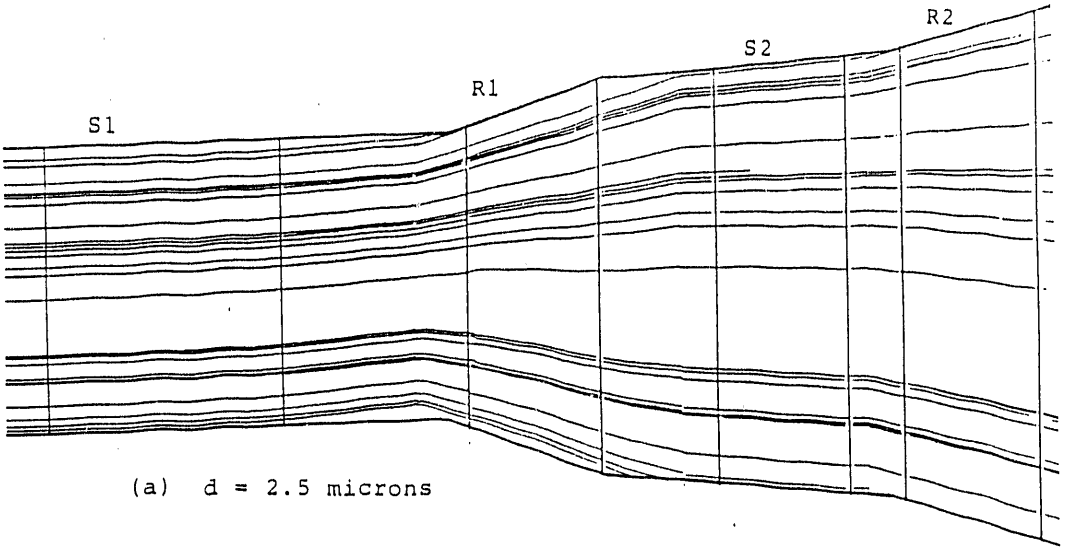

(a) d = 2.5 microns

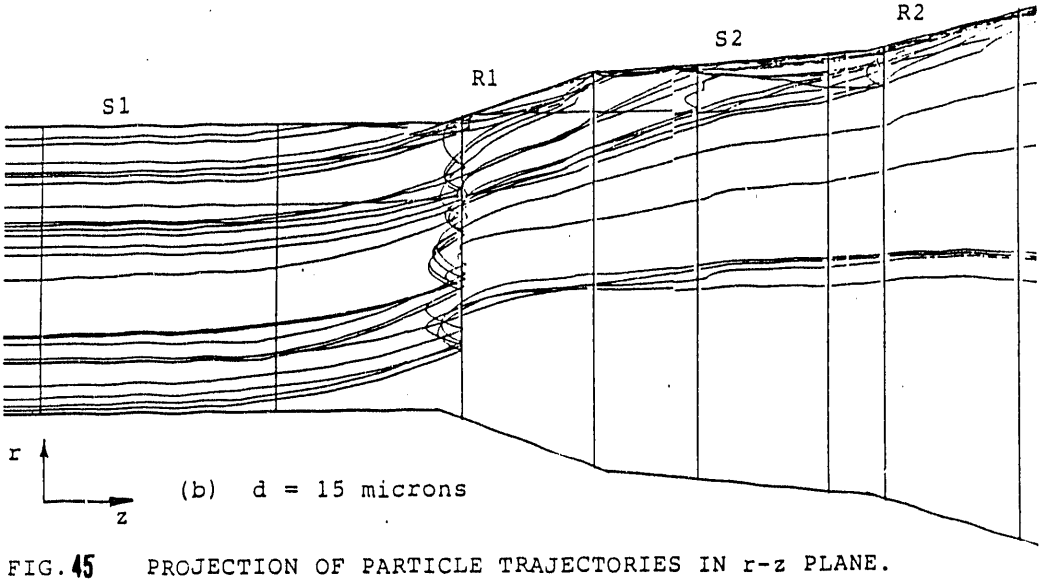

(b) d = 15 microns

FIG. 45 PROJECTION OF PARTICLE TRAJECTORIES IN r-z PLANE.

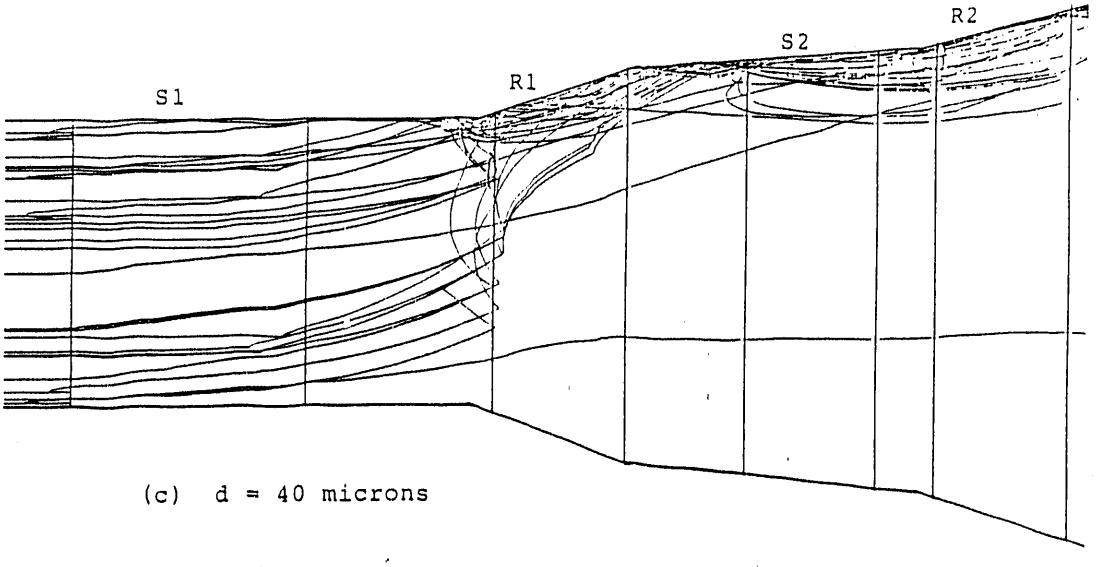

(c) d = 40 microns

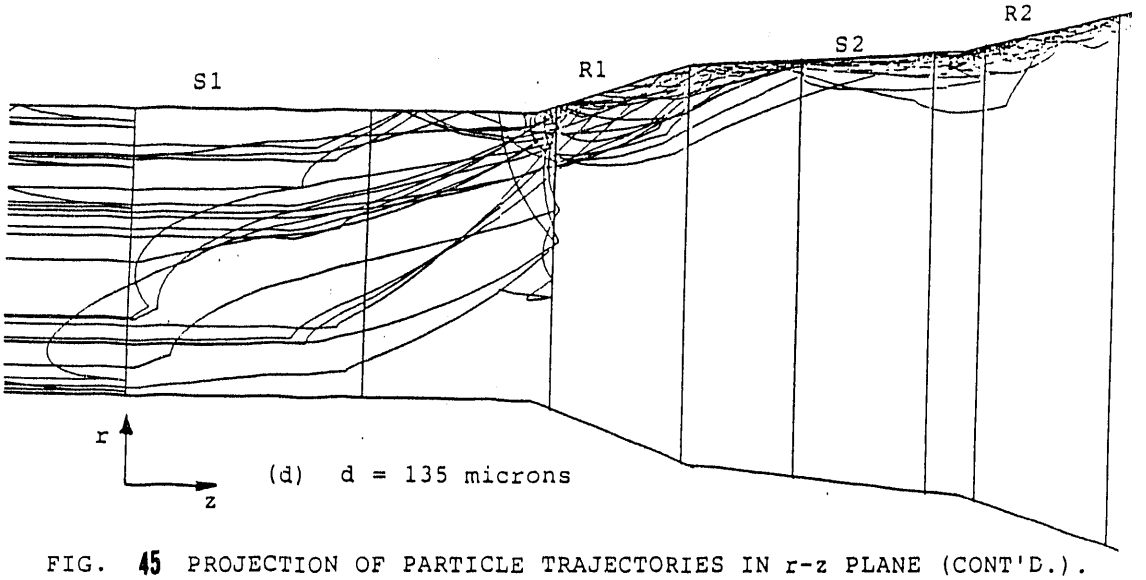

(d) d = 135 microns

FIG. 45 PROJECTION OF PARTICLE TRAJECTORIES IN r-z PLANE (CONT'D.).

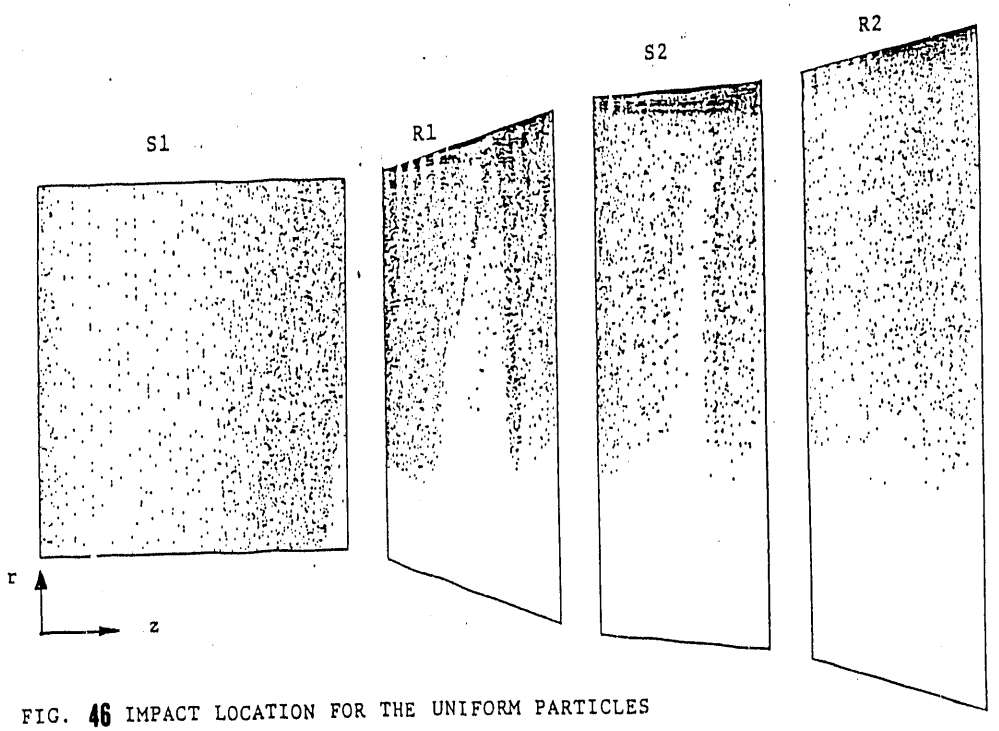

FIG. 46 IMPACT LOCATION FOR THE UNIFORM PARTICLES

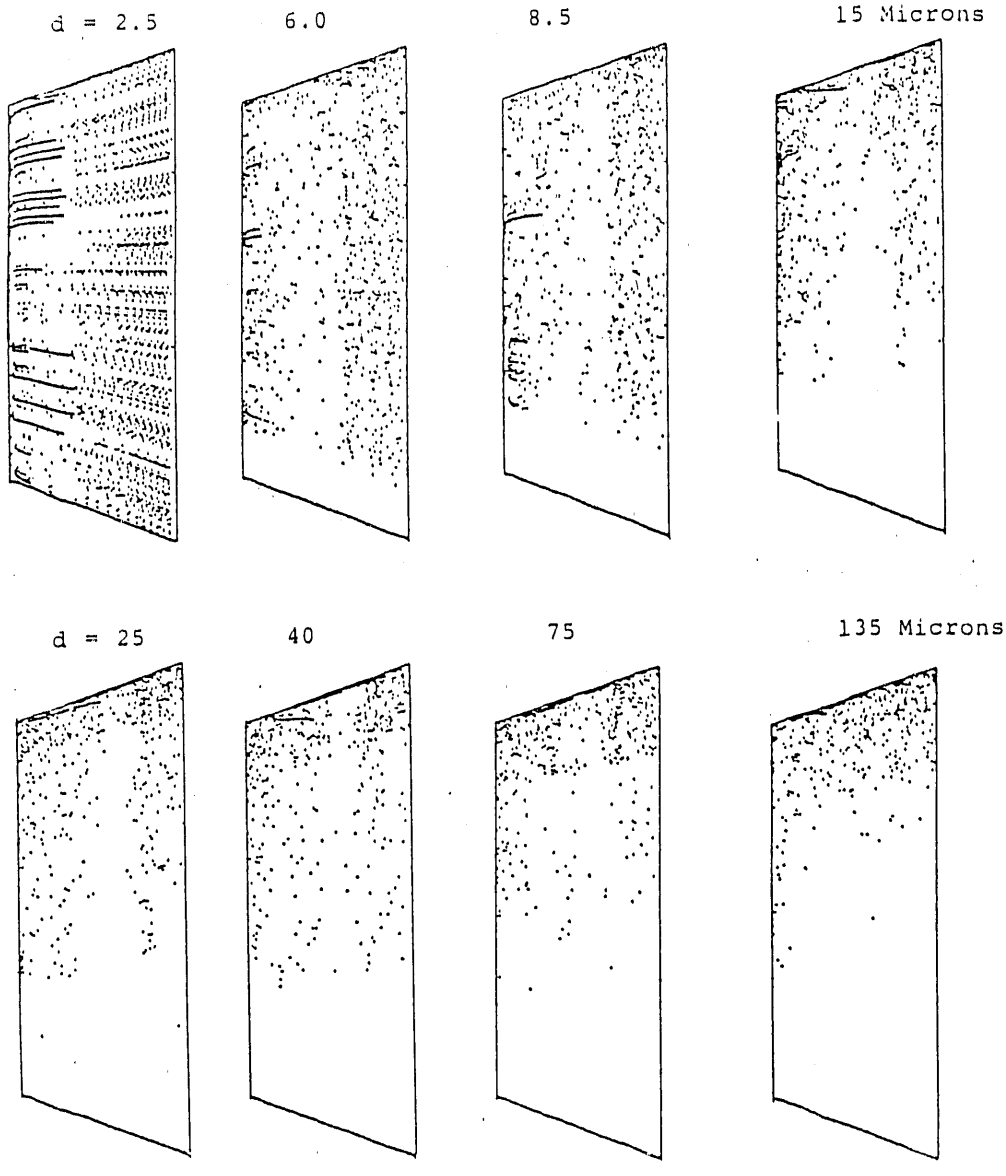

FIG. 47 IMPACT LOCATIONS FOR THE INDIVIDUAL PARTICLE SETS FIRST ROTOR.

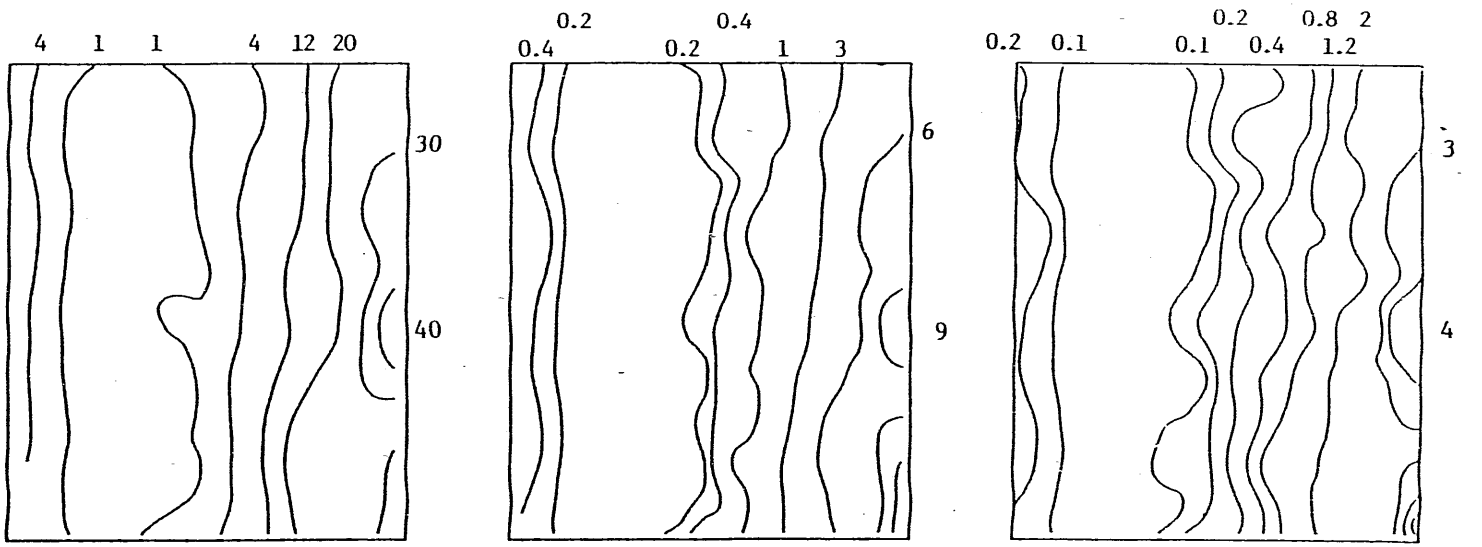

(a) M246 ALLOY
Nickel Base Alloy

(b) N COATING
Aluminide Coating
(Substrate M246)

(c) RT22 COATING
Platinum Aluminide Coating
(Substrate M246)

FIG. 48. FIRST STATOR PRESSURE SURFACE EROSION RATE x 10^5 (mgm/gm/cm^2)

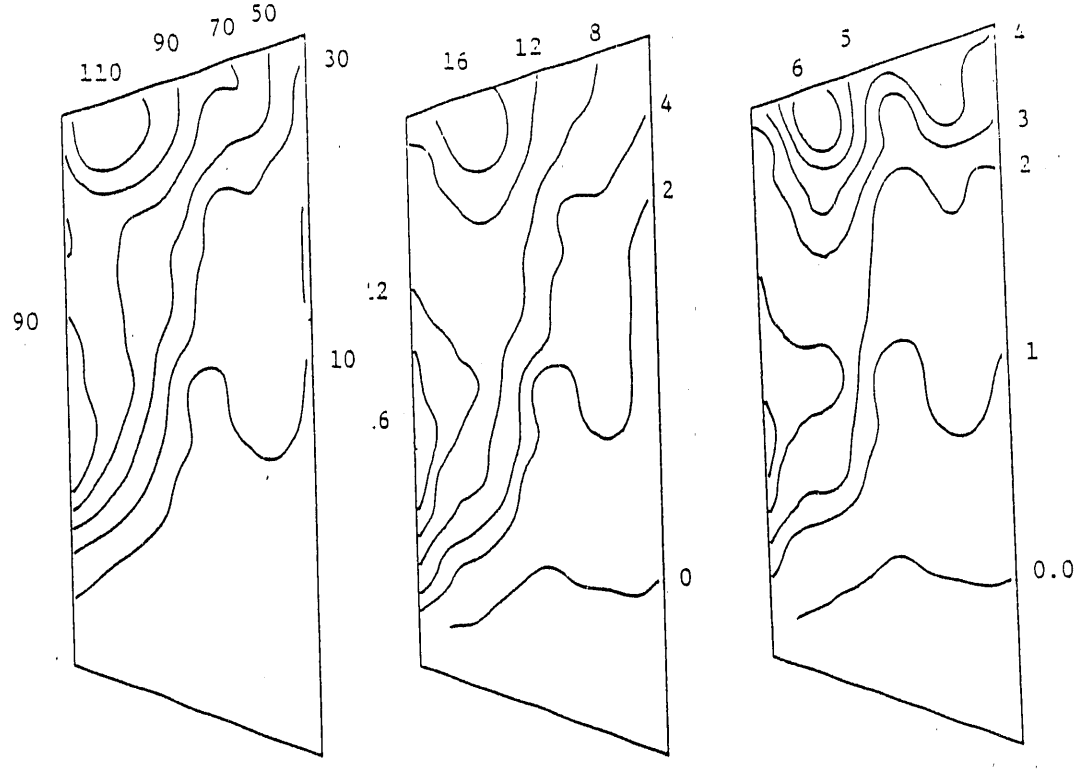

(a) M246 ALLOY (b) N COATING (c) RT22 COATING

FIG. 49. FIRST ROTOR PRESSURE SURFACE EROSION RATE x 10^5 (mgm/gm/cm^2)

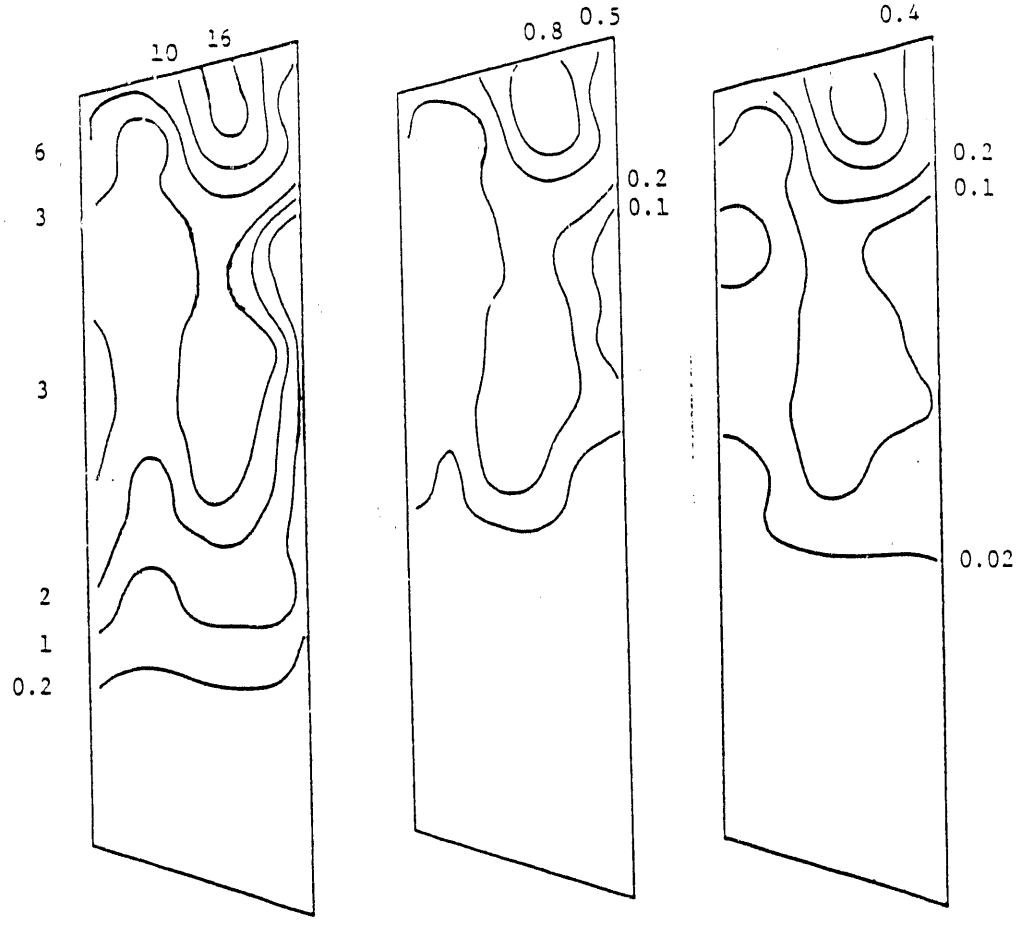

(a) M246 ALLOY (b) N COATING (c) RT22 COATING

FIG. 50. SECOND ROTOR PRESSURE SURFACE EROSION RATE x 10^5 (mgm/gm/cm^2)

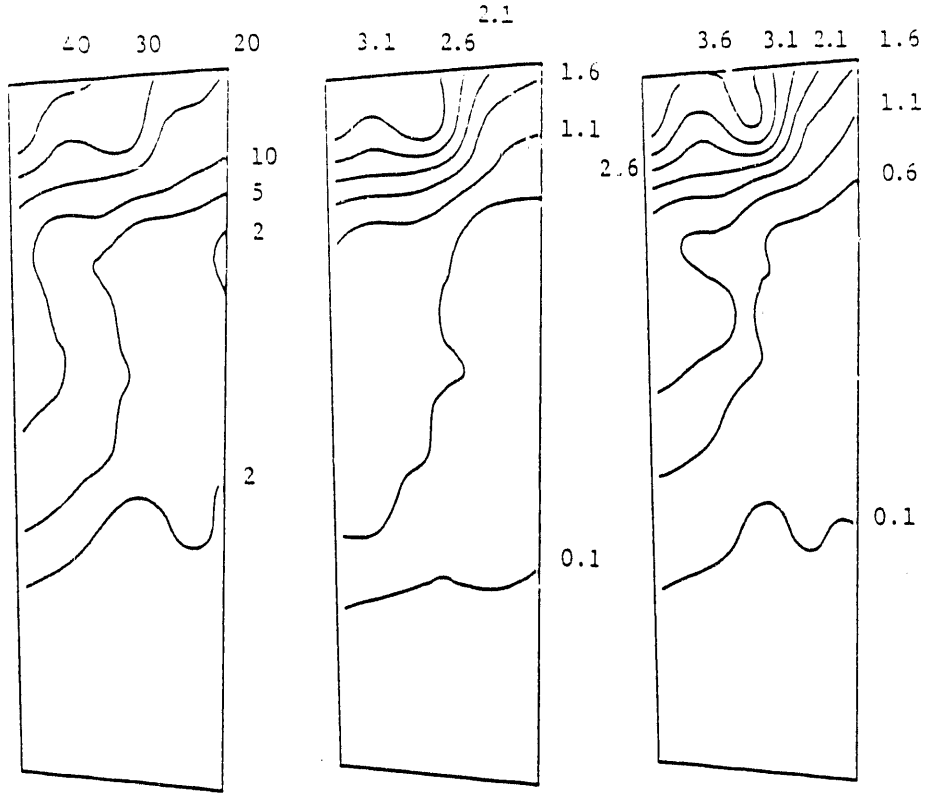

(a) M246 ALLOY (b) N COATING (c) RT22 COATING

FIG. 51. SECOND STATOR PRESSURE SURFACE EROSION RATE x 10^5 (mgm/gm/cm^2)

DISTRIBUTION

AIR PRODUCTS AND CHEMICALS
P.O. Box 538
Allentown, PA 18105
S. W. Dean
S. C. Weiner

ARGONNE NATIONAL LABORATORY
9700 S. Cass Avenue
Argonne, IL 60439
W. A. Ellingson
K. Natesan

AVCO RESEARCH LABORATORY
2385 Revere Beach Parkway
Everett, MA 02149
R. J. Pollina

BABCOCK & WILCOX
1562 Beeson St.
Alliance, OH 44601
T. I. Johnson
T. Modrak

BABCOCK & WILCOX
Domestic Fossil Operations
20 South Van Buren Avenue,
Barberton, OH 44023
M. Gold

BABCOCK & WILCOX
Lynchburg Research Center
P.O. Box 11165
Lynchburg, VA 24506
H. Moeller

BATTELLE-COLUMBUS LABORATORIES
505 King Avenue
Columbus, OH 43201
I. G. Wright

BRITISH COAL CORPORATION
Coal Research Establishment
Stoke Orchard, Cheltenham
Glochester, England GL52 4RZ
M. Arnold
C. Bower
A. Twigg

BRITISH GAS CORPORATION
Westfield Development Centre
Cardenden, Fife,
Scotland KY5OHP
J. E. Scott

BROOKHAVEN NATIONAL LABORATORY
Department of Applied Science,
Upton, Long Island, NY 11973
T. E. O'Hare

CANADA CENTER FOR MINERAL & ENERGY TECHNOLOGY
568 Booth Street
Ottawa, Ontario
Canada K1A OG1
R. Winston Revie
Mahi Sahoo

COMBUSTION ENGINEERING
1000 Prospect Hill Road
Windsor, CT 06095
D. A. Canonico

CONSOLIDATION COAL COMPANY
4000 Brownsville Road
Library, PA 15129
S. Harding

ELECTRIC POWER RESEARCH INSTITUTE
P.O. Box 10412
3412 Hillview Avenue
Palo Alto, CA 94303
W. T. Bakker
J. Stringer

EUROPEAN COMMUNITIES JOINT RESEARCH CENTRE
Petten Establishment
P.O. Box 2
1755 ZG Petten
The Netherlands
M. Van de Voorde

FLUIDIZED BED TECHNOLOGIES
P. O. Box 4469
Chattanooga, TN 37405
R. Q. Vincent

FOSTER WHEELER DEVELOPMENT CORPORATION
Materials Technology Department
John Blizard Research Center
12 Peach Tree Hill Road
Livingston, NJ 07039
J. L. Blough

GAS RESEARCH INSTITUTE
8600 West Bryn Mawr Avenue
Chicago, IL 60631
H. S. Meyer

GENERAL ELECTRIC COMPANY
1 River Road,Bldg. 55, Room 115
Schenectady, NY 12345
R. W. Haskell

GEORGIA INSTITUTE OF TECHNOLOGY
Georgia Tech Research Institute
Atlanta, GA 30332
T. L. Starr

LAWRENCE BERKELEY LABORATORY
University of California
Berkeley, CA 94720
A. V. Levy

LAWRENCE LIVERMORE LABORATORY
P.O. Box 808, L-325
Livermore, CA 94550
W. A. Steele

MOBIL RESEARCH & DEVELOPMENT CORPORATION
P. O. Box 1026
Princeton, NJ 08540
R. C. Searles

NATIONAL INSTITUTE OF STANDARDS AND TECHNOLOGY
Materials Building
Gaithersburg, MD 20899
L. K. Ives

NATIONAL MATERIALS ADVISORY BOARD
National Research Council
2101 Constitution Avenue
Washington, DC 20418
K. M. Zwilsky

NEW ENERGY AND INDUSTRIAL TECHNOLOGY DEVELOPMENT ORGANIZATION
Sunshine 60 Bldg.
P.O. Box 1151
1-1, Higashi-Ikebukuro 3-chrome
Toshima-Ku
Tokyo, 170
Japan
H. Narita
S. Ueda

OAK RIDGE NATIONAL LABORATORY
P.O. Box 2008
Oak Ridge, TN 37831
P. J. Blau
P. T. Carlson
N. C. Cole
R. R. Judkins
J. R. Keiser
R. A. Lawson (8 copies)

RISOE NATIONAL LABORATORY
P.O. Box 49
DK-4000, Roskilde
Denmark
Aksel Olsen

SHELL DEVELOPMENT COMPANY
P. O. Box 1380
Houston, TX 77251-1380
L. W. R. Dicks

TENNESSEE VALLEY AUTHORITY
Energy Demonstration & Technology
MR 2N58A
Chattanooga, TN 37402-2801
C. M. Huang

TENNESSEE VALLEY AUTHORITY
1101 Market Street
3A Missionary Ridge
Chattanooga, TN 37402-2801
A. M. Manaker

UNIVERSITY OF CALIFORNIA AT BERKELEY
Department of Mechanical Engineering
Berkeley. CA 94720
J. A. C. Humphrey

UNIVERSITY OF NOTRE DAME
Department of Materials Science and Engineering
P.O. Box E
Notre Dame. IN 46556
T. H. Kosel

WESTERN RESEARCH INSTITUTE
365 N. 9th Street
P.O. Box 3395
University Station
Laramie, WY 82071
V. K. Sethi

WESTINGHOUSE ELECTRIC CORPORATION
Research and Development Center
1310 Beulah Road
Pittsburgh. PA 15235
S. C. Singhal

WESTINGHOUSE HANFORD COMPANY
P.O. Box 1970
W/A-65
Richland. WA 99352
R. N. Johnson

DOE
DOE OAK RIDGE FIELD OFFICE
P. O. Box 2001
Oak Ridge, TN 37831
Assistant Manager for Energy Research and Development

DOE
DOE OAK RIDGE FIELD OFFICE
P. O. Box 2008
Building 4500N, MS 6269
Oak Ridge, TN 37831
E. E. Hoffman

DOE
OFFICE OF BASIC ENERGY SCIENCES
Materials Sciences Division
ER-131, GTN
Washington, DC 20545
J. B. Darby

DOE
OFFICE OF FOSSIL ENERGY
Washington, DC 20545
J. P. Carr (FE-14) GTN

DOE
MORGANTOWN ENERGY TECHNOLOGY CENTER
P.O. Box 880
Morgantown, WV 26505
R. A. Bajura
R. C. Bedick
D. C. Cicero
F. W. Crouse, Jr.
N. T. Holcombe
W. J. Huber
M. J. Mayfield
J. E. Notestein
J. S. Wilson

DOE
PITTSBURGH ENERGY TECHNOLOGY CENTER
P.O. Box 10940
Pittsburgh, PA 15236
A. H. Baldwin
G. V. McGurl
R. Santore
T. M. Torkos

END

DATE FILMED

7/29/92